



CHALMERS
UNIVERSITY OF TECHNOLOGY

Valorization of hazardous graphite from black mass (NMC 111) of lithium-ion battery recycling via KOH activation for functional carbon

Downloaded from: <https://research.chalmers.se>, 2025-05-28 21:06 UTC

Citation for the original published paper (version of record):

Dziejarski, B., Arevalo Fester, J., Serafin, J. et al (2025). Valorization of hazardous graphite from black mass (NMC 111) of lithium-ion battery recycling via KOH activation for functional carbon design. *Materials and Design*, 254. <http://dx.doi.org/10.1016/j.matdes.2025.114073>

N.B. When citing this work, cite the original published paper.



Valorization of hazardous graphite from black mass (NMC 111) of lithium-ion battery recycling via KOH activation for functional carbon design

Bartosz Dziejarski^{a,b,c,*}, Jose Eduardo Arevalo Fester^a, Jarosław Serafin^d,
Martina Petranikova^a, Eric Tam^e, Anna Martinelli^f, Renata Krzyżyńska^c, Klas Andersson^b,
Pavleta Knutsson^a

^a Department of Chemistry and Chemical Engineering, Division of Energy and Materials, Chalmers University of Technology, SE-412 96 Gothenburg, Sweden

^b Department of Space, Earth and Environment, Division of Energy Technology, Chalmers University of Technology, SE-412 96 Gothenburg, Sweden

^c Faculty of Environmental Engineering, Wrocław University of Science and Technology, 50-370 Wrocław, Poland

^d Department of Inorganic and Organic Chemistry, University of Barcelona, Martí i Franquès, 1-11, 08028 Barcelona, Spain

^e Department of Industrial and Materials Science, Division of Materials and Manufacture, Chalmers University of Technology, SE-412 96 Gothenburg, Sweden

^f Department of Chemistry and Chemical Engineering, Division of Applied Chemistry, Chalmers University of Technology, SE-412 96 Gothenburg, Sweden

ARTICLE INFO

Keywords:

LIBs
Graphite recovery
Activated carbon
Carbon-based materials
Circular economy
Resource valorization

ABSTRACT

The rapid adoption of lithium-ion batteries (LiBs) in energy storage has driven research into resource recovery. This study converts hazardous graphite from the black mass (NMC 111) of spent LiBs into functional activated carbons (ACs) via KOH activation. Tailoring the synthesis at 800 °C and a graphite-to-KOH ratio of 1:6 produced AC with a surface area of 678 m²/g and a total pore volume of 0.442 cm³/g. The material showed a balanced micropore–mesopore structure, with micropores contributing 53 % of the total pore volume. The material showed a balanced micropore–mesopore structure, with micropores contributing 53 % of the total volume. XRD confirmed preserved graphitic crystallinity with a dominant (002) peak at 26.52°. Raman spectroscopy indicated increased defect density ($I_D/I_G = 1.053$), facilitating porosity formation. SEM and TEM revealed a transition from smooth graphite layers to a porous, defect-rich structure, with TEM highlighting mesopore-like voids and distorted graphitic domains featuring edge defects. XPS identified surface modifications, including a higher proportion of sp² carbon and oxygen-containing groups (C–O, C=O, C–OH, CO₃²⁻). TGA demonstrated stability (~900 °C) under inert conditions and enhanced reactivity in oxidative environments. This work valorizes LiB-derived graphite waste into ACs, supporting circular economy strategies and demonstrating potential for industrial scalability.

1. Introduction

Over the past decade, lithium-ion batteries (LiBs) have been at the forefront of energy storage innovations, driving transformative changes across numerous industries, particularly in transportation and renewable energy integration [1,2]. The extensive integration of Li-ion batteries in electric vehicles (EVs) has positioned them as a key technology in the global transition toward sustainable, low-carbon energy systems [3]. The widespread adoption of electric vehicles was evident in 2023 when nearly 14 million electric cars were sold globally, representing 18

% of the total car sales, a significant increase if compared to the 14 % level in 2022. As the trend continues, electric car sales are projected to climb further, potentially reaching around 17 million in 2024, i.e. more than one in five cars sold worldwide [4]. This transition from internal combustion engines to battery-powered alternatives has led to decreased greenhouse gas emissions (220 Mt in 2023 compared to 80 Mt in 2022) [4], cleaner transportation and improved air quality [5]. Furthermore, the demand for LiBs extends beyond the automotive industry, including larger-scale stationary energy storage systems that support renewable energy integration and grid stability [6,7]. As renewable energy sources

* Corresponding author at: Department of Chemistry and Chemical Engineering, Division of Energy and Materials, Chalmers University of Technology, SE-412 96 Gothenburg, Sweden.

E-mail address: bartoszd@chalmers.se (B. Dziejarski).

<https://doi.org/10.1016/j.matdes.2025.114073>

Received 16 March 2025; Received in revised form 23 April 2025; Accepted 6 May 2025

Available online 9 May 2025

0264-1275/© 2025 The Author(s). Published by Elsevier Ltd. This is an open access article under the CC BY license (<http://creativecommons.org/licenses/by/4.0/>).

such as solar and wind power become more prevalent, the need for efficient energy storage to address intermittent energy supply will grow correspondingly [8]. Projections indicate that the demand for LiBs is anticipated to grow by approximately 33 % annually, reaching an estimated 4.7 GWh by 2030 [9].

Even though it contributes to the decrease of environmental impact of the transport and energy sector, the rapid expansion of LiBs introduces new challenges related to their short lifecycle, typically spanning the range of 3–8 years. The main challenge is connected to the end-of-life (EoL) management, where over 2 million tons of spent LiBs are projected to be generated annually [10]. LiBs are complex electrochemical systems containing a mix of valuable secondary resources, such as lithium (Li), cobalt (Co), nickel (Ni), manganese (Mn), and copper (Cu), which are essential for battery performance and can be recovered for reuse [11]. However, they also contribute to hazardous waste generation, encompassing electrolyte residues, fluorinated compounds, and toxic metals such as lead and cadmium, which can pose serious environmental and health hazards if not effectively controlled [12]. A LiB cell comprises approximately 25 wt% casing materials (steel and plastics), ~27 wt% cathode materials (e.g., LiCoO_2 , LiFePO_4 , LiNiCoMnO_2), 12–17 wt% anode materials (graphite), ~13 wt% current collectors (Cu and Al), 10–15 wt% electrolyte (such as LiPF_6 or LiBF_4 dissolved in dipolar organic solvents), ~4 wt% separator (polypropylene), and ~4 wt% binder (polyvinylidene difluoride) [13,14]. Among the most prominent batteries in production, nickel manganese cobalt (NMC)-based LiBs have cathodes composed of a mixture of Li, Ni, Mn, and Co, such as $\text{LiNi}_{0.6}\text{Mn}_{0.2}\text{Co}_{0.2}\text{O}_2$ (NMC 622), $\text{LiNi}_{0.8}\text{Mn}_{0.1}\text{Co}_{0.1}\text{O}_2$ (NMC 811), and $\text{LiNi}_{1/3}\text{Mn}_{1/3}\text{Co}_{1/3}\text{O}_2$ (NMC 111). Notably, NMC 111 has garnered significant attention as a cathode material for next-generation LiBs due to its numerous advantages, including lower cost compared to LiCoO_2 , high theoretical capacity, low toxicity, excellent thermal stability, and superior energy density [15].

Lithium, cobalt, and nickel are key elements for enhancing battery performance, longevity, and energy density [16]. The EU Battery Directive anticipates an improvement in Li-ion battery recycling efficiency, increasing from 50 % in 2006 to 65 % by 2025 [17]. This advancement aims to close the material loop by recovering valuable metals, with Ni and Co being the main economic incentives driving LiBs recovery efforts. The recently introduced European Battery Regulation sets ambitious recovery targets: lithium recovery is expected to reach 50 % by 2027 and 80 % by 2031, while Co, Cu, Pb, and Ni are targeted at 90 % by 2027 and 95 % by 2031 [18]. Achieving these goals, however, is challenging due to the complex composition and diverse materials within LiBs, which require multiple preparatory steps before processing. The initial stages involve classification, discharge or inactivation, disassembly, and material separation. These processes prepare the batteries for subsequent treatment using direct recycling, pyrometallurgy, or hydrometallurgy [19]. Due to the legislative requirements, hydrometallurgy is and will be the preferred method for the recycling. This brings the challenges for the recyclers to deal with the significant amount of waste graphite since its application is limited and moreover it is considered to be a hazardous waste. Current EoL strategies typically begin with discharge and mechanical pre-treatment, followed by optional pyrolysis to remove organic components. The subsequent steps, including sorting and pre-processing, result in a sieved mixture of cathode powders and anode graphite, commonly referred to as black mass (BM) [20]. Processing BM focuses on extracting valuable transition metals while isolating and purifying graphite from the anode. Historically overlooked, graphite has only recently been recognized as a recoverable and valuable resource, further enhancing the economic and environmental benefits of LiB recycling [21].

Graphite continues to dominate as the preferred anode material in commercial LiBs, primarily due to its outstanding cycling stability, high electrical conductivity, and mechanical flexibility. With approximately 1 kg of graphite required per kWh of battery capacity, which is 10 to 20 times more than lithium, its demand has driven the market to a value of

\$29.05 billion by 2022 [22]. Beyond its role in batteries, graphite's unique combination of electrical conductivity, thermal stability and structural versatility also makes it an ideal precursor for advanced material synthesis [23–25]. One promising research path involves using recovered graphite as a precursor for activated carbons (ACs), a class of porous materials with extensive environmental applications due to their high specific surface area, tunable pore structure, low cost, and thermal and chemical stability [26,27]. ACs are widely used in, for example, gas separation and storage [28], water purification [29], energy storage [30], and as catalyst supports in chemical processes [31]. The synthesis of ACs typically involves activation processes applied to precursor materials to optimize their textural and structural properties. Among the commonly used chemical activating agents (including KOH, K_2CO_3 , H_3PO_4 , and ZnCl_2), KOH stands out as the most promising activator resulting in high-quality ACs with a large pore volume, abundant surface oxygen functional groups, and dominant microporosity [32,33]. The effectiveness of KOH, likewise the other activators, is significantly influenced by the chosen activation parameters, which vary depending on the raw material. Among the multiple activation parameters, activation temperature (500–900 °C) and mass ratio between the activator and precursor (1:1–1:7) are reported to have the most substantial impact on the resulting AC properties [34,35].

While traditional precursors such as biomass, coal, or petroleum-derived polymers have been widely explored, they often require intensive energy input and may yield materials with inconsistent properties [36–38]. In contrast, graphite recovered from spent lithium-ion batteries exhibits a high fixed carbon content, partial graphitization, and intrinsic electrical conductivity, which not only facilitates the formation of well-developed porosity during activation but also reduces the activation energy required [39]. These favorable physicochemical properties enable the synthesis of high-performance activated carbons with lower process energy demands. Moreover, the presence of residual metal species and surface defects in the recovered graphite can further promote pore development. From a cost perspective, although the initial collection and purification of black mass involves logistical and technical challenges, the use of this industrial waste stream circumvents the need for virgin raw materials, making it a more economically attractive and sustainable solution in the long term [20]. From a circular economy perspective, valorizing black mass diverts hazardous waste from landfills and simultaneously creates value-added materials suitable for energy and environmental applications. Despite the growing interest in ACs derived from waste materials, the potential of graphite recovered from LiBs as a precursor for AC synthesis has not received significant attention. Nonetheless, a two studies have explored graphite nanofibers (GNFs) as a carbon source for activation. For example, Meng et al. [40] investigated the effect of heat treatment (700–1000 °C) on the activation of GNFs using KOH. Similarly, Yuan et al. [41] prepared porous GNFs (PGNFs) through KOH activation, varying the GNF/KOH weight ratio from 0 to 5 at 900 °C. In view of this, investigating the use of recovered graphite as a precursor for ACs is particularly relevant in the context of sustainable waste management and the transition to a circular economy. Transforming waste graphite into high-value ACs addresses three critical challenges: reducing the environmental impact of LiB disposal, recovering graphite as an essential raw material, and creating functional materials that promote economic sustainability.

This study explores the transformation of graphite recovered from industrial black mass (NMC 111) of spent lithium-ion batteries into ACs through chemical activation using KOH. The research focuses on uncovering the underlying mechanisms that lead to structural, textural, and chemical changes during the activation process. Following the mechanism provides a comprehensive understanding of how waste-derived graphite can be converted into high-performance porous materials. A wide array of advanced characterization techniques was employed to investigate the evolution of properties in the activated carbons. These techniques include nitrogen adsorption/desorption isotherms for textural analysis, Raman spectroscopy and X-ray diffraction

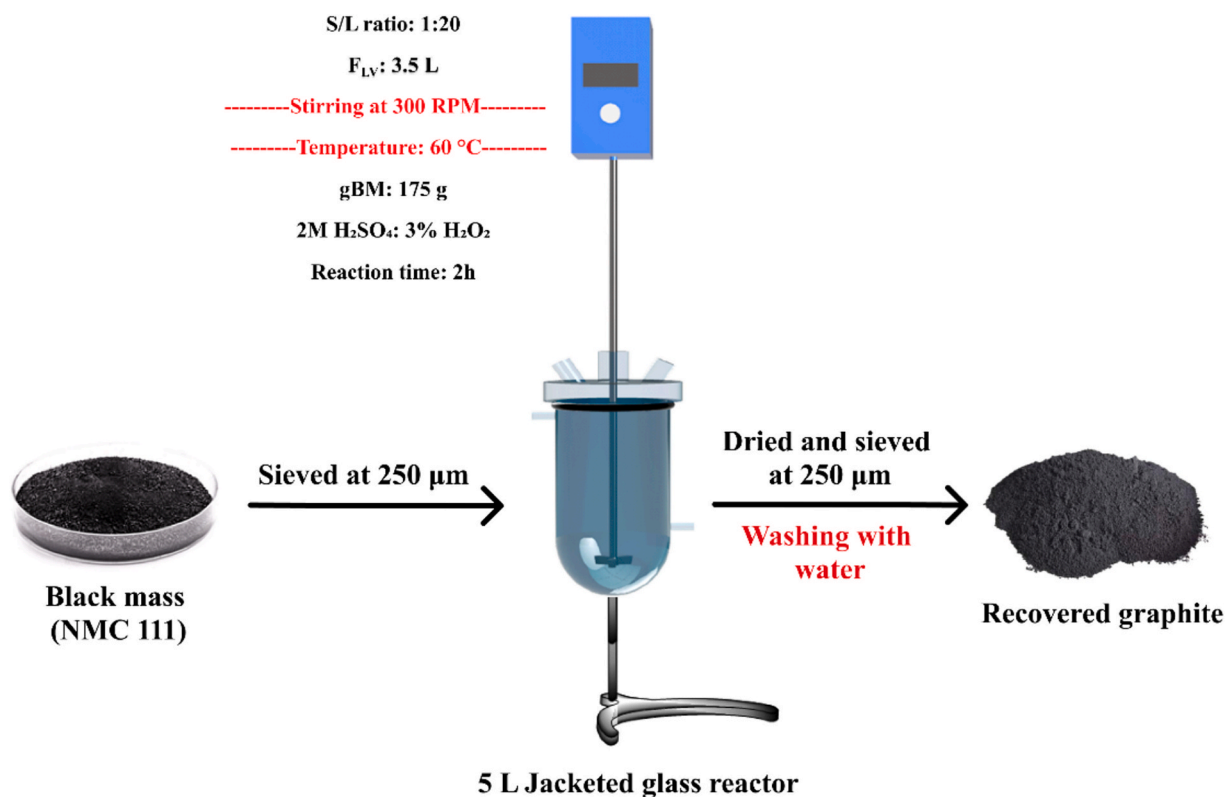


Fig. 1. A schematic representation illustrating the preparation steps utilized for the leaching of industrial black mass (NMC 111) to enable graphite recovery.

(XRD) for structural evaluation, and scanning electron microscopy (SEM), transmission electron microscopy (TEM), and energy-dispersive X-ray spectroscopy (EDS) for morphological and compositional studies. Furthermore, X-ray photoelectron spectroscopy (XPS) was used to examine the chemical modifications, specifically focusing on the introduction of functional groups and the changes in bonding states, while thermogravimetric analysis (TGA) assessed the thermal behavior and stability of the materials. The novelty of this work lies in its detailed investigation of the chemical activation process of recovered graphite, providing the first mechanistic insights into its transformation into activated carbons. The study uniquely addresses the interplay between activation conditions, such as temperature and KOH-to-graphite ratio, and their effects on the resulting material properties. This research not only contributes to advancing resource recovery strategies for spent LiBs but also highlights the potential for developing sustainable, high-value waste materials, thereby supporting the principles of a circular economy.

2. Materials and methods

2.1. Black mass

The black mass was obtained after disassembling 150 kg of battery packs from Volvo Cars AB (Sweden). Packs were discharged by Volvo Cars AB and disassembled by Stena Recycling AB (Sweden). Then, the 120 kg of the cells (NMC 111) were mechanically treated and separated by Akkuser Oy (Finland), at temperatures below 50 °C. Obtained black mass was further sieved to under 500 µm at the Industrial Materials Recycling group at Chalmers University of Technology (Sweden) to achieve a highly concentrated homogeneous powder. Carbon content of the black mass was 32 wt%.

2.2. Leaching of industrial black mass (NMC 111)

The overall procedure, illustrating the preparation steps for the leaching of industrial black mass to enable graphite recovery, is presented in Fig. 1.

In a 5 L glass-jacketed reactor equipped with a mechanical stirrer, 2 L of deionized water and 392.8 mL of 95 % H₂SO₄ were introduced portion-wise, followed by an additional 929.3 mL of deionized water. The reactor temperature was set to 60 °C. While stirring at 300 RPM, 175 g of black mass, previously sieved to 250 µm, was gradually incorporated. Finally, 178 mL of 59 % H₂O₂ was introduced portion-wise to prevent overflow from the formation of black foam. The final concentrations of H₂SO₄ and H₂O₂ were 2 M and 3 %, respectively, maintaining a solid-to-liquid ratio of 1:20 with a final liquid volume of 3.5 L. After 2 h of reaction, stirring was stopped, and the slurry was poured into a 4 L beaker for vacuum filtration. The black solid was washed with deionized water until the pH reached 7. Approximately 80 g of the solid was then transferred to a 4 L beaker, and 2 L of deionized water was added. The mixture was stirred at 300 RPM for 60 min. Subsequently, the slurry was filtered, washed with deionized water, and dried overnight at 60 °C. Finally, the dried solid was crushed in a mortar and sieved again to 250 µm. Recovered graphite was obtained after this sieving process, which effectively reduced the plastic content originating from Li-ion battery separators.

XRF analysis, as shown in Table S1, confirmed the removal of most metal impurities after leaching, including complete elimination of P (0.340 wt%). Trace amounts of Ni (0.118 wt%), Co (0.261 wt%), and Mn (0.331 wt%) remained in the recovered graphite, while Si (0.364 wt %) appeared despite being undetected in the original black mass, likely due to washing-related contamination. The low residual transition metal content suggests minimal catalytic influence during activation. In contrast to conventional graphite, LiB-derived precursors require additional purification due to their complex composition (active material residues, binders, and additives), but they offer potential for tuning the

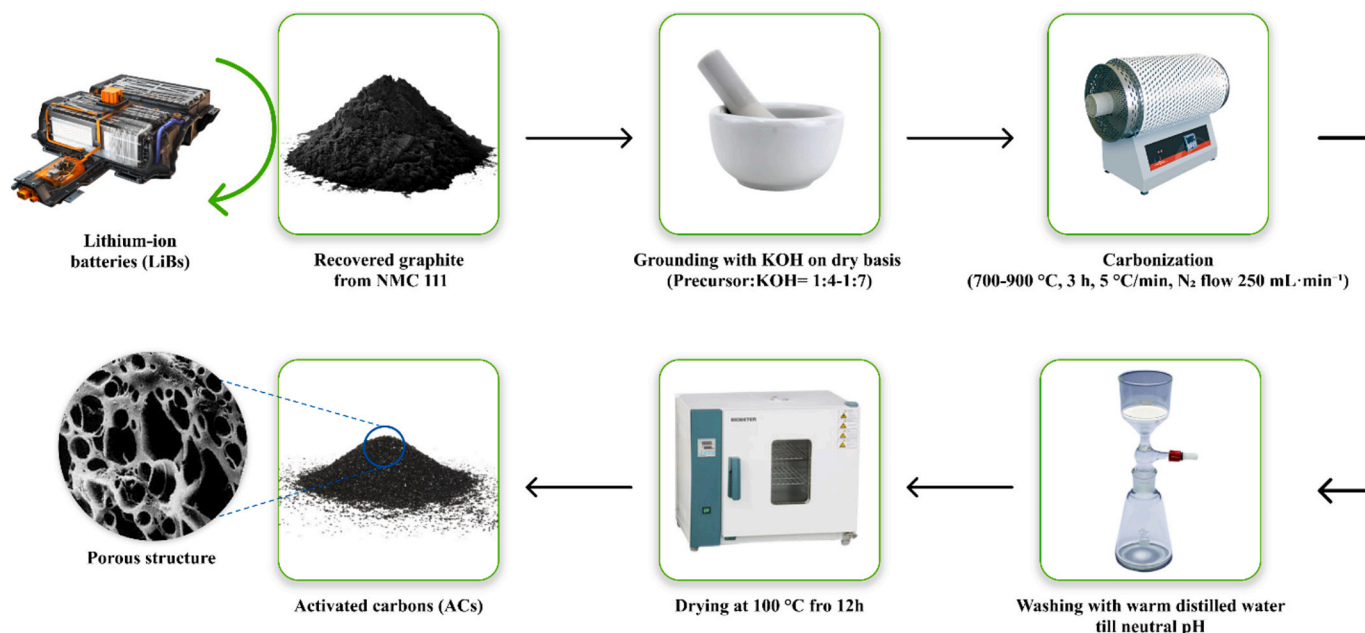


Fig. 2. Methodology for preparation procedures used for KOH activation of recovered graphite from NMC 111.

properties of activated carbon materials.

2.3. Preparation of activated carbons

Activated carbons were synthesized from the recovered graphite through chemical activation using KOH in a dry mixing process, as presented in Fig. 2 and Table S2. The specific mass amounts of graphite and KOH were ground together in a mortar to create a uniform solid mixture which was placed in a horizontal furnace.

Activation was performed under an inert nitrogen atmosphere with a constant flow rate of $250 \text{ mL}\cdot\text{min}^{-1}$. Two activation parameters were examined: temperature and the graphite to KOH ratio. The temperatures were set at $700 \text{ }^\circ\text{C}$, $800 \text{ }^\circ\text{C}$, and $900 \text{ }^\circ\text{C}$, each maintained for 3 h, based on preliminary studies and reported literature confirming the adequacy of this duration, with a heating rate of $5 \text{ }^\circ\text{C}\cdot\text{min}^{-1}$. An initial graphite to KOH ratio of 1:4 was used as a baseline to assess the stages of KOH activation behavior. This ratio was further modulated at the optimal temperature ($800 \text{ }^\circ\text{C}$) to enhance the textural properties, adjusting from ratios of 1:5 up to 1:7. The resulting ACs were washed multiple times with deionized water until the washing water reached a constant pH. Finally, all samples were dried in an oven at $100 \text{ }^\circ\text{C}$ for 24 h. The activated carbon samples were labeled as AC-X_Z, where X represents the activation temperature, and Z represents the graphite to KOH ratio.

2.4. Characterization of carbon-based materials

2.4.1. Textural characterization

The textural properties of the synthesized ACs were assessed using N_2 adsorption isotherms measured at $-196 \text{ }^\circ\text{C}$. The analysis was performed using fully automated Tristar II 3020 Micromeritics, a surface area and porosity analyzer with three stations. Before testing, the samples were degassed by sequential heating to $90 \text{ }^\circ\text{C}$ for 4 h, followed by $250 \text{ }^\circ\text{C}$ for 16 h. A total of approximately 61 adsorption/desorption points were recorded across a relative pressure (P/P_0) range from $1\cdot 10^{-4}$ to ~ 0.98 . The maximum volume of nitrogen gas adsorbed during the analysis was $25 \text{ cm}^3/\text{g STP}$.

The specific surface area was evaluated using the Brunauer-Emmett-Teller (S_{BET}) method within a P/P_0 range of 0.05 to 0.3, then adjusted according to the modified BET approach by Rouquerol et al. [42], ensuring the highest linear correlation ($R^2 \approx 1$). The total pore volume

(V_{TOT}) was evaluated at a high relative pressure, typically around 0.99 or higher. The pore size distribution (PSD), as well as the micropore (V_{MIC}) and mesopore (V_{MES}) volumes, were determined using the non-local density functional theory (NLDFT) model, assuming a slit-shaped pore structure within the density functional theory (DFT) framework.

2.4.2. Structural and surface characterization

The lattice structural changes during the transformation from NM 111 to ACs were investigated using XRD analysis with a Bruker D8 Discover diffractometer. Prior to analysis, the samples were ground to a fine powder and mounted on a zero-background sample holder to minimize interference. The measurements were conducted using the $\text{Cu K}\alpha$ radiation ($\lambda = 1.5406 \text{ \AA}$). The recorded spectra were analyzed using the DIFFRAC.EVA and PDF 4 + databases. Additionally, based on the XRD data, graphitic structural parameters were calculated for the recovered graphite and the synthesized ACs [43–45]. The mean crystallite thickness (L_c) and the mean graphene sheet diameter (L_a) were calculated using the Scherrer equation [46]:

$$L_{c,a} = K\lambda / (\beta \cos\theta) \quad (1)$$

where:

L_c is the average crystallite thickness [nm], where the (002) signal was used with $K = 0.89$,

L_a is the average graphene sheet diameter [nm], where (110) signal was applied with $K = 1.84$.

K is a constant specific to the reflection plane,

λ is the X-ray wavelength (0.154 nm for Cu),

β is the peak width at half maximum intensity (110 or 002), corrected for instrumental broadening (0.07121 rad) using the Warren method [47] and assuming Gaussian peak shapes [rad].

θ is the diffraction angle [rad].

The average interlayer spacing between the graphitic layers (d_{002}) was calculated using Bragg's law [48]:

$$d_{002} = n\lambda / (2\sin\theta) \quad (2)$$

where n is the diffraction order (typically $n = 1$).

Finally, the number of graphene sheets (N) was estimated as [49]:

$$N = L_c / d \quad (3)$$

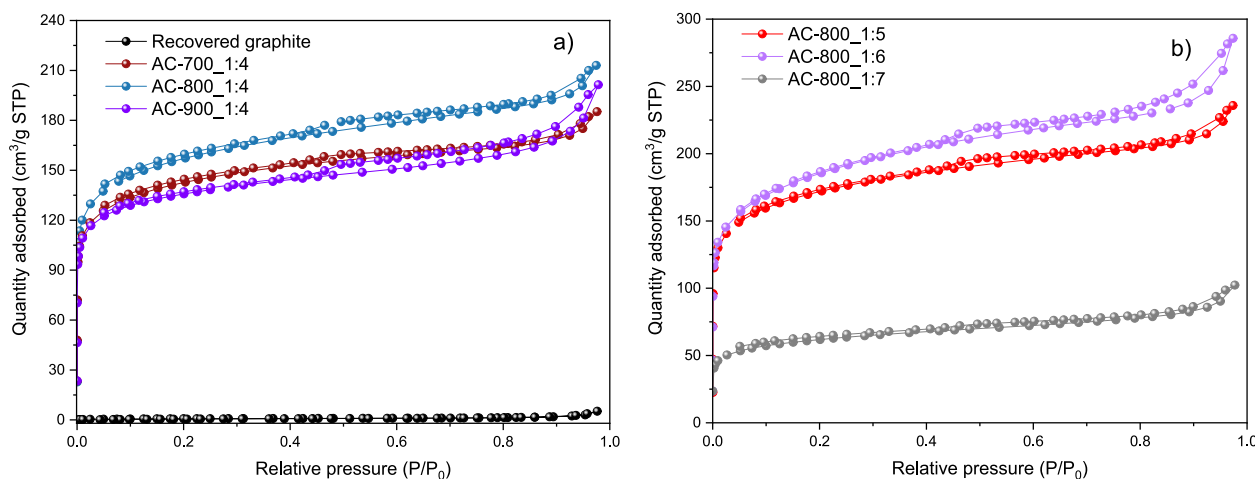


Fig. 3. N_2 adsorption–desorption isotherms at $-196\text{ }^\circ\text{C}$ for the prepared ACs illustrating the effects of (a) varying temperatures (700–900 $^\circ\text{C}$) and (b) different mass ratios between recovered graphite and KOH (1:5–1:7).

Surface chemical composition and the chemical states of the determined elements were analyzed using an X-ray photoelectron spectroscopy (PHI5000 VersaProbe III – Scanning XPS Microprobe™). To handle non-conductive samples, dual charge compensation was employed by running both Ar ion gun (+ve) and electron neutralizer (–ve) during measurements. Survey scan in an energy range between 0 and 1300 eV with the step size of 1.0 eV was first carried out to assess the overall elemental composition. With the elements identified, narrow scans (0.1 eV step size) were conducted at the selected regions to determine the chemical states of the elements of interest. The spectral peak's energy resolution was determined to be 0.673 eV (full width at half maximum, FWHM) based on the Ag $3d_{5/2}$ peak measurement from a sputter-cleaned silver (Ag) foil. The energy scale was calibrated following the ISO 15472 standard, aligning the core-level spectra of sputter-cleaned gold (Au $4f_{7/2}$), silver (Ag $3d_{5/2}$), and copper (Cu $2p_{3/2}$) at 83.96 eV, 368.21 eV, and 932.62 eV, respectively.

Raman spectra were collected using an InVia Raman spectrometer from Renishaw. An Ar-ion laser, 532 nm and 100 mW of maximum power at the source, was used as the excitation source coupled with a Peltier-cooled CCD detector and a grating with 2400 l/mm. The spectral resolution was better than 2 cm^{-1} and the spectral range $100\text{--}4000\text{ cm}^{-1}$ was covered. Before any measurement, the spectrometer was calibrated to the first order line of a Si wafer at 520.6 cm^{-1} . Raman spectra were recorded on different spots using 1 % of the nominal power (to avoid overheating and hence damage of the sample), accumulating for 10 s during 10 accumulations. The spectra were presented in their original. Background subtraction was applied to enhance the clarity of the spectral features, and cosmic ray artifacts were removed during data processing to ensure the reliability of the results. The analysis aimed to evaluate the structure of the carbon skeleton in the obtained carbon materials, such as the degree of graphitization or the presence of defects.

Elemental composition was determined using an energy-dispersive X-ray fluorescence spectrometer (EDXRF, Epsilon 3 type, PANalytical B.V.) to assess the removal of metal impurities before and after leaching.

2.4.3. Thermogravimetric characterization

Thermogravimetric analysis was performed using a Mettler Toledo TGA-DSC 3 + thermal analyzer to evaluate the thermal stability and decomposition behavior of the materials. The samples were heated from $30\text{ }^\circ\text{C}$ to $900\text{ }^\circ\text{C}$ at a rate of 10 K/min under both N_2 and air atmospheres. The influence of oxidative and inert conditions on material degradation was monitored through the mass loss profile during continuous heating.

2.4.4. Morphological characterization

A scanning electron microscopy (FEI ESEM Quanta 200) equipped

with energy-dispersive X-ray spectroscopy was used to determine the morphological changes of the samples. Imaging was conducted using the backscattered electron (BSE) signal. To prevent surface charging, the microscope was operated in low vacuum mode at a pressure of 20 Pa, with an electron beam acceleration voltage of 10 kV.

Transmission electron microscopy was used to examine the microstructure of the samples, focusing on lattice ordering, pore formation, and edge morphology. Imaging was carried out using a Titan 80–300 microscope (FEI) equipped with a field emission gun, a monochromator (0.11 eV energy resolution for EELS), and a Gatan 866 GIF Tridiem energy filter. A spherical aberration corrector enabled high-resolution TEM imaging with a spatial resolution down to 70 pm, and fast Fourier transform (FFT) analysis was applied to assess structural disorder and lattice features.

3. Results and discussion

3.1. Effect of KOH activation on the textural properties of recovered graphite

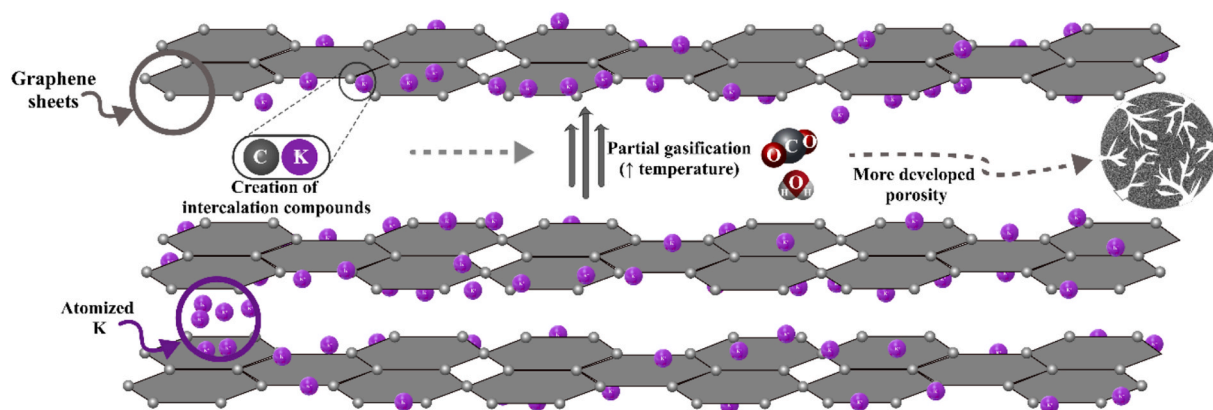
Fig. 3(a, b) presents the N_2 adsorption/desorption isotherms of activated carbons produced at temperatures ranging from 700 to 900 $^\circ\text{C}$ and with mass ratios of graphite to KOH between 1:5 and 1:7. The isotherms show a rapid uptake at low relative pressures ($P/P_0 < 0.1$), confirming that the ACs are predominantly microporous, while the hysteresis loops indicate the presence of secondary mesoporosity. This result aligns with expectations, as KOH activation is well known to produce micropores due to its chemical etching and widening effects on the carbon matrix. Additionally, it was noticed that the amount of N_2 adsorbed increased with the rise in thermal treatment temperature and the recovered graphite:KOH ratio during carbon sample preparation, reaching its maximum at 800 $^\circ\text{C}$ with a ratio of 1:6.

According to the International Union of Pure and Applied Chemistry (IUPAC) classification, the N_2 sorption isotherms shown in Fig. 3(a, b) display Type Ib at low P/P_0 values and Type IVa behavior at medium and higher relative pressures [50]. Type Ib is typical for microporous materials with a broader pore size distribution, encompassing wider micropores and possibly narrow mesopores ($< \sim 2.5\text{ nm}$). The sharp uptake at very low P/P_0 values (< 0.015) is attributed to strong N_2 -ACs interactions and is linked to the progressive filling of micropores [51]. Conversely, the Type IVa isotherm is characteristic of mesoporous materials. It begins with monolayer-multilayer adsorption on the mesopore walls, following a similar path to the corresponding portion of a Type II isotherm, and is then followed by capillary condensation [52]. In the case of a Type IVa isotherm, capillary condensation occurring in wider

Table 1

The textural properties of ACs produced at different temperatures and different graphite:KOH ratios and using recovered graphite from NMC 111.

Sample	BET surface area ^a , [m ² /g]	Total pore volume ^b , [cm ³ /g]	Micropore volume ^c , [cm ³ /g]	Mesopore volume ^c , [cm ³ /g]	Micropore volume/total pore volume, [%]	Mesopore volume/total pore volume, [%]	Yield, [%]	Burn off, [%]
Recovered graphite	3 ± 0.06	0.008	–	–	–	–	–	–
AC-700_1:4	531 ± 1.95	0.286	0.191	0.095	67	33	58.6	41.4
AC-800_1:4	583 ± 2.37	0.329	0.200	0.129	61	39	54.8	45.2
AC-900_1:4	514 ± 1.14	0.312	0.182	0.130	58	42	48.1	51.9
AC-800_1:5	633 ± 3.13	0.364	0.222	0.142	61	39	53.5	46.5
AC-800_1:6	678 ± 1.09	0.442	0.233	0.209	53	47	51.2	48.8
AC-800_1:7	228 ± 0.64	0.158	0.083	0.075	53	47	45.3	54.7

^a BET method using the Rouquerol criteria.^b V_{TOT} was determined from the N₂ adsorption isotherm at a high relative pressure (~0.98–0.99).^c DFT method by the NLDFT model.**Fig. 4.** Schematic illustration of the sequence of potassium intercalation into graphitic layers and the formation of porosity.

mesopores (> 4 nm) results in hysteresis. The observed Type H4 hysteresis suggests the presence of slit-shaped pores, consistent with structures containing limited amounts of mesopores constrained by surrounding micropores [53].

The textural properties of all ACs and recovered graphite from NMC 111, including BET surface area, total pore volume, and micropore and mesopore volumes, as determined by N₂ sorption measurements, are summarized in Table 1. From the different activation temperatures, the sample prepared at 800 °C (AC-800_1:4) demonstrated the most favorable textural characteristics: specific surface area of 583 m²/g, total pore volume of 0.329 cm³/g, and a balanced distribution between micropores and mesopores. The micropore volume reached 0.200 cm³/g, while the mesopore volume measured 0.129 cm³/g, accounting for 61 % and 39 % of the total pore volume, respectively. When the mass ratio between recovered graphite and KOH was varied at 800 °C, the AC-800_1:6 sample showed superior textural properties, combining a high surface area with a balanced micro- and mesopore structure. This sample achieved the S_{BET} of 678 m²/g and the largest V_{TOT} of 0.442 cm³/g, with mesopores contributing with 47 %. The increase in V_{MES} is particularly notable, suggesting that adjusting by increasing to a certain degree the graphite-to-KOH ratio enhances mesopore development, which is beneficial for applications involving larger molecule adsorption or faster diffusion rates. However, the AC-800_1:7 produced with a higher KOH dosage, exhibited significantly lower S_{BET} (228 m²/g) and V_{TOT} (0.158 cm³/g), highlighting the detrimental effect of over-etching. Although higher KOH ratios enhance chemical etching via redox and gasification reactions, excessive activation as observed for the 1:7 ratio leads to pore wall thinning, shrinkage, and partial collapse of the carbon framework [54]. This over-etching effect results in a paradoxical reduction in both specific surface area and mesopore volume, as reflected further in the broadening of the PSD and the decrease in cumulative pore volume

(Fig. S1) [55]. Additionally, the narrowing of mesopores is indicated by the shift and weakening of the hysteresis loop in the desorption branch of the N₂ isotherm. Finally, the yield of AC samples varies depending on the activation conditions, with values ranging from 45.3 % to 58.6 %, indicating that a higher KOH ratio and temperature lead to greater mass loss during activation. This trend suggests that increasing the temperature and KOH ratio enhances the etching effect, leading to more extensive removal of carbonaceous material and consequently lower yield.

The efficiency of KOH activation of recovered graphite at 800 °C can be attributed to the formation of metallic potassium. At temperatures above 760 °C, metallic K forms during heat treatment, intercalates into the graphitic layers, and diffuses into the internal structure of the carbon particles [56]. This process generates new porosity or expanding existing pores within the graphite structure (Fig. 4) [33]. At higher temperatures, these changes intensify due to the increased activity and mobility of K atoms. Consequently, KOH activation can be described in three main stages, with the final stage being the formation of metallic K. The first stage involves the partial gasification of carbon, where reactive gases such as CO₂ and H₂O are generated, contributing to the development of porosity. The second stage occurs at temperatures exceeding 700 °C, where the formation of K-species promotes etching of the carbon skeleton, thereby creating the pore framework through redox reactions [57]. These species contribute to the breakdown of the carbon matrix, promoting the formation of porosity during the thermal activation process [58,59]. Further XRD analysis of unwashed AC-800_1:6 confirmed the presence of various K-containing species formed during KOH activation, supporting the proposed multi-step activation mechanism and highlighting the role of in situ-generated K species in pore development. Finally, between 800 °C and 900 °C, the S_{BET}, V_{TOT}, and V_{MIC} decreased, while the V_{MES} remained similar to that at 800 °C.

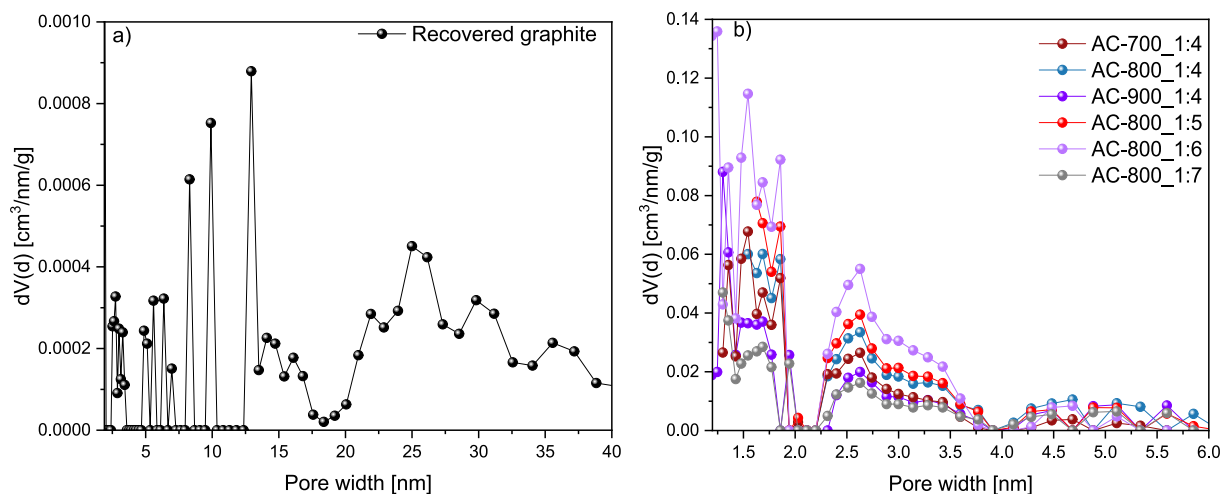


Fig. 5. Pore size distribution of (a) recovered graphite and (b) activated carbons at different temperatures and graphite:KOH ratios, calculated on the basis of N_2 adsorption by using DFT method.

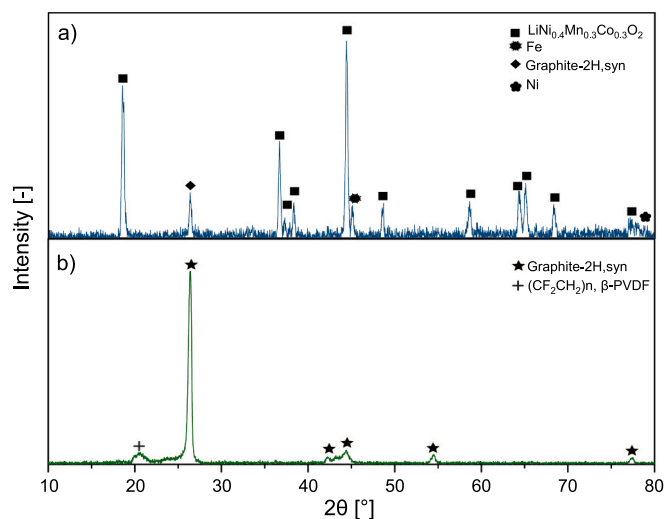


Fig. 6. XRD patterns of (a) NMC 111 and (b) unwashed graphite after leaching.

Although mesopore formation still occurs at higher temperatures, prolonged exposure can lead to partial collapse or damage of the porous network, thereby reducing the overall surface area and limiting pore accessibility [60,61].

Fig. 5(a, b) illustrates the pore size distribution of recovered graphite and ACs. The porosity of graphite was found to be very low, consisting mainly of mesopores, with primary peaks concentrated between 5 nm and 15 nm, and sharp, distinct spikes around 6 nm, 8 nm, and 10 nm. In contrast, the PSD analysis reveals that the ACs obtained were predominantly microporous and mesoporous, with higher content of pore sizes up to 2 nm. It should be noted that significant peaks were observed between 1.2 and 2 nm, with a particular concentration below 1 nm, reflecting the presence of developed narrow micropores. Due to their kinetic diameter, nitrogen molecules are unsuitable for accurately determining the pore volume of pores smaller than 1 nm; however, the cumulative pore volume curve indicates their presence [62]. Additionally, mesopores up to 6 nm were identified, with the majority concentrated between 2.2 and 4 nm, as indicated by a pronounced peak at 2.6 nm. A secondary distribution was also evident in the 4 to 6 nm range.

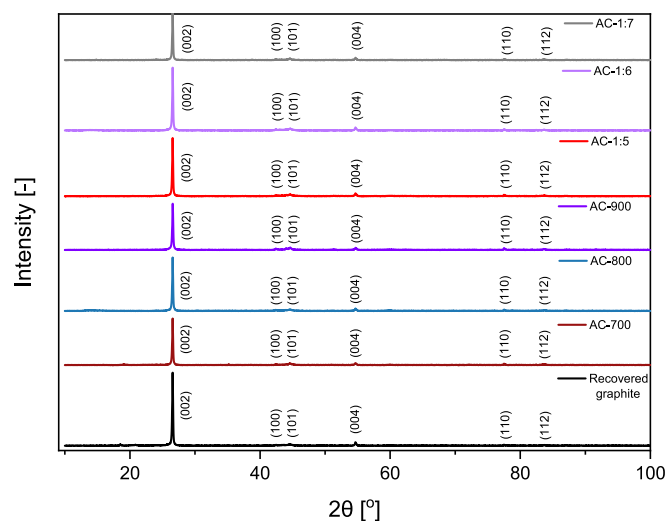


Fig. 7. XRD patterns of recovered graphite after washing and synthesized ACs at different temperatures and various graphite:KOH ratios. The crystallographic planes corresponding to the peaks are also indicated.

3.2. Structural transformations: From NMC 111 to activated carbons

Fig. 6 presents the XRD diffractograms of (a) NMC 111 and (b) unwashed graphite after leaching of NMC 111. The XRD pattern of the pristine NMC 111 reveals peaks corresponding to an intermediary mixture of active components from Li-ion battery wastes. The peaks attributed to $LiNi_{0.4}Mn_{0.3}Co_{0.3}O_2$ reflect the layered structure of the cathode active material, while additional peaks for crystalline graphite confirm the presence of anode material [63,64]. Minor peaks corresponding to metallic Fe and Ni are also observed, which likely originate as impurities or secondary phases inherent to the black mass composition [65].

By comparing Fig. 6(a) and (b), it becomes evident that the leaching process effectively dissolves a portion of the metallic content while retaining the graphite. The XRD pattern of unwashed recovered graphite after the leaching of NMC 111 exhibits a dominant peak at 2 theta of 26.52° , indicating the retention of its highly crystalline structure during the leaching process. Additionally, a minor peak at 21° , associated with polyvinylidene fluoride (PVDF), a polymeric binder material used to attach the cathode materials to aluminum, is also observed [66]. These observations suggest that while the leaching process was effective in

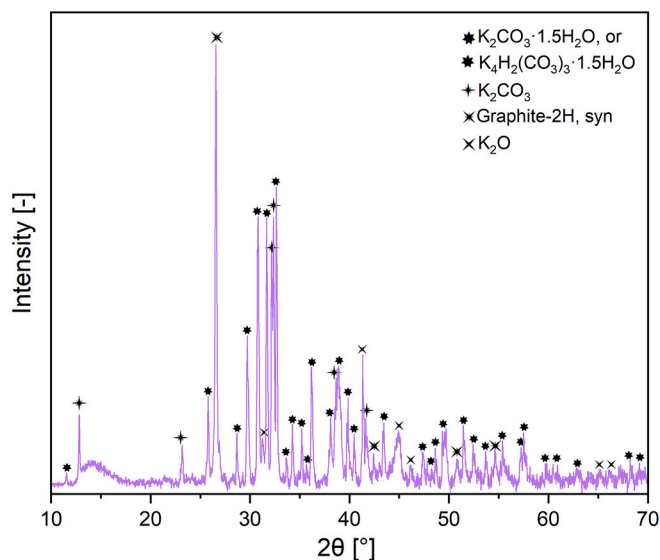


Fig. 8. XRD diffractogram of AC-800_1:6 before washing treatment.

recovering the graphite, some semicrystalline plastic phases remain. However, subsequent water washing further reduced these residues, indicating the effectiveness of this additional purification step, as shown in Fig. 7.

Fig. 7 presents the XRD patterns of the recovered graphite after washing with water, as well as the prepared AC samples. The recovered graphite washed with water and synthesized activated carbons exhibit characteristic peaks at 26.52°, 42.38°, 44.62°, 54.66°, 77.52°, and 83.64°, corresponding to the (002), (100), (101), (004), (110), and (112) crystal planes, respectively. These findings are consistent with values reported in the literature (ICDD card No. 41–1487) [67]. The preservation of characteristic peaks in recovered graphite and ACs confirms that KOH activation does not alter the graphite crystal structure. The sharp diffraction peaks show that the long-range order of the hexagonal layers remains intact, with no changes in interlayer spacing or stacking. This demonstrates that KOH activation improves textural properties while maintaining structural integrity during thermochemical conversion.

Moreover, based on the XRD pattern of the unwashed activated carbon sample (AC-1:6) after KOH activation of recovered graphite, several crystalline phases have been identified, including potassium carbonate hydrates ($K_2CO_3 \cdot 1.5H_2O$, $K_4H_2(CO_3)_3 \cdot 1.5H_2O$), potassium carbonate (K_2CO_3), graphite (Graphite-2H), and potassium oxide (K_2O). Fig. 8 provides insight into the potential reactions occurring during the activation process, highlighting the formation of K-based residues and the incomplete removal of activation by-products [68].

- Reaction of recovered graphite with KOH

During high-temperature activation, potassium hydroxide reacts with graphite (C), leading to the formation of potassium compounds and gaseous by-products (H_2 , H_2O , CO , CO_2). This process consists of several simultaneous reactions that introduce porosity into the carbon structure while depositing K_2CO_3 and K_2O as residues. These reactions can be described in two generic ways, as outlined below:



K_2CO_3 may mainly form via the direct interaction of K_2O with CO_2 :



Table 2

The average values of d_{002} , L_c , L_a , and N.

Sample	d_{002} [nm]	L_c [nm]	L_a [nm]	N [-]
Recovered graphite	0.335	50.401	154.391	145
AC-700_1:4		49.630	212.2	148
AC-800_1:4		48.660	249.359	145
AC-900_1:4		45.074	174.491	135
AC-800_1:5		49.447	189.587	148
AC-800_1:6		49.045	253.286	146
AC-800_1:7		51.153	194.041	153

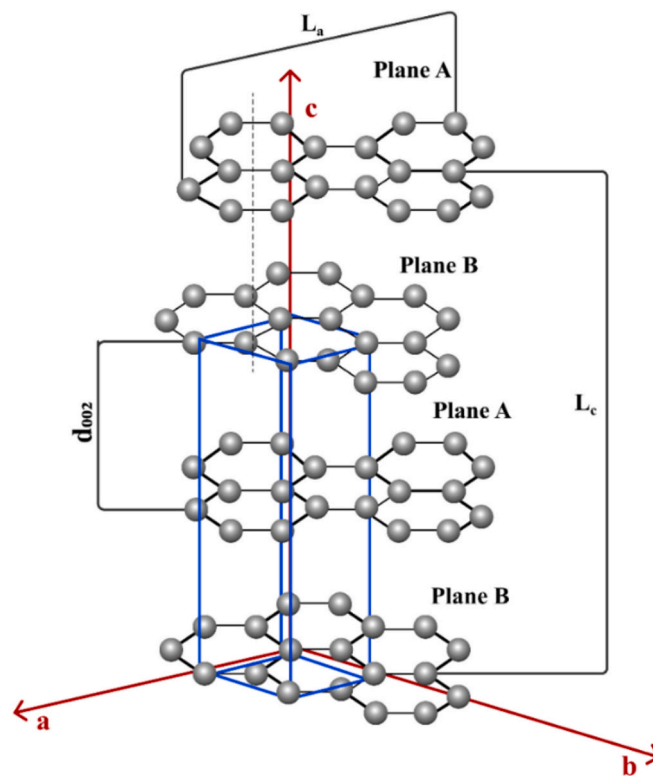


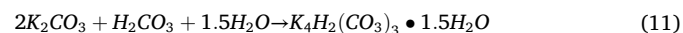
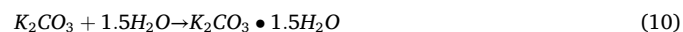
Fig. 9. Visualization of graphitic structural parameters (L_a , L_c , d_{002}) for recovered graphite and synthesized ACs.

K_2O arises independently, primarily due to the thermal decomposition of KOH and K_2CO_3 or the reaction of K with CO_2 :



- Formation of potassium carbonate hydrates

During cooling and exposure to ambient moisture, K_2CO_3 can absorb water, leading to the formation of hydrated potassium carbonate phases:



These phases suggest that moisture absorption occurred post-activation, possibly during handling.

- Presence of graphite

Despite the activation process, some graphite (Graphite-2H) is still

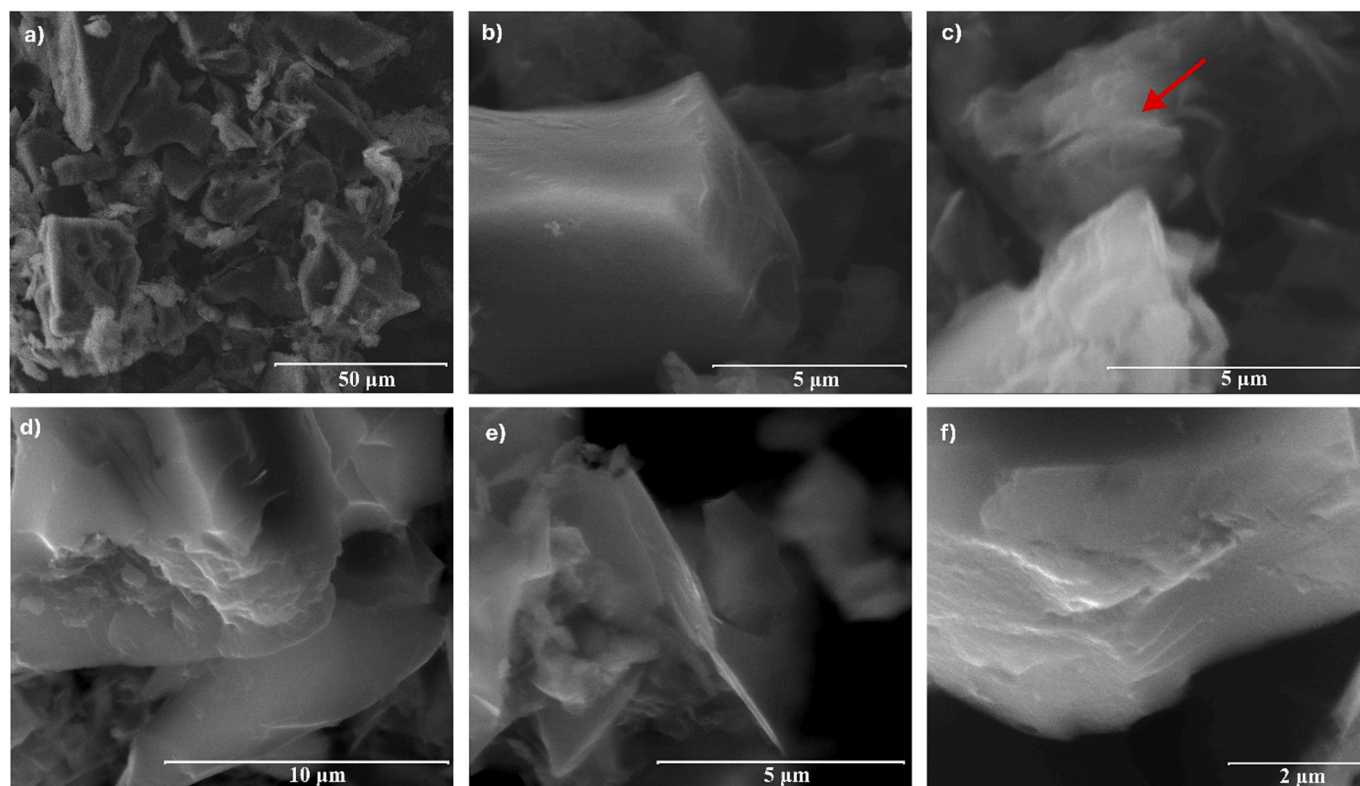


Fig. 10. SEM micrographs of (a–c) recovered graphite from NMC 111, showing the overall structure with distinct, plate-like particles (a), smooth and well-defined edges (b), and stacked graphitic layers within a single particle (c, red arrow); and (d–f) AC-800_1:6, displaying an irregular and porous structure with voids and cavities (d), a fragmented structure (e), and a rough surface (f). (For interpretation of the references to colour in this figure legend, the reader is referred to the web version of this article.)

visible in the XRD pattern, suggesting retention of graphitic layers within the AC structure.

Table 2 presents the structural parameters of recovered graphite and synthesized ACs, including d_{002} , L_c , L_a , and N , respectively. These parameters are further visualized in Fig. 9. The d_{002} value remains constant at 0.335 nm across all samples, indicating that the KOH treatment does not alter the fundamental spacing between graphene sheets, as discussed before. In contrast, L_c decreases with increasing temperatures (49.630–45.074 nm), suggesting a progressive reduction in the vertical alignment of graphene layers within the graphite structure. Notably, samples with higher KOH ratios, such as AC-800_1:6 and AC-800_1:7, tend to exhibit stable or slightly increased L_c , reflecting variations in the degree of structural preservation under these conditions. To further support the interpretation of structural changes, the FWHM of the (002) peak was calculated and is summarized in Table S3, offering a quantitative measure of peak broadening and structural disorder. Slight variations in FWHM align with the observed trends in L_c , where broader peaks generally correspond to reduced stacking heights along the c-axis.

L_a values show significant variability, with the highest values observed for AC-800_1:4 ($L_a = 249.359$) and AC-800_1:6 ($L_a = 253.286$). These increases suggest that, under certain conditions, the process supports the expansion of lateral crystallite dimensions, corresponding to the in-plane domains of graphene. Conversely, at elevated temperatures, such as for AC-900_1:4 ($L_a = 174.491$), L_a decreases, likely due to fragmentation and structural breakdown. However, no clear dependence on temperature or KOH ratio is observed, as L_a fluctuates probably due to variations in the treatment process affecting graphene sheet dimensions. Finally, the number of graphene layers decreases with rising activation temperatures, as observed in AC-900_1:4 ($N = 135$), reflecting the thinning of graphite stacks at higher temperatures. For samples with varying KOH proportions, the ratio itself does not significantly affect the stacking order or layer thickness.

3.3. Role of KOH activation in morphological changes

Fig. 10(a, b, c) depicts SEM images of the recovered graphite from NMC 111. The micrographs reveal distinct, plate-like particles with well-defined edges, characteristic of graphite's layered, crystalline structure. The smooth surfaces and sharp boundaries indicate the orderly stacking of graphene sheets, with minimal porosity, surface roughness, or voids. Additionally, the integrity of the layered arrangement of graphitic layers is prominently visible, which contributes to the high structural order of material [69]. In contrast, the SEM micrographs of the AC sample (AC-800_1:6), as shown in Fig. 10(d, e, f), reveal a substantial morphological transformation compared to the pristine recovered graphite precursor. The structure appears irregular and porous, as a result of the KOH activation process. During this process, carbon atoms are removed from the graphite structure, introducing defects and irregularities [70]. The surface roughness of the particles has noticeably increased, with the formation of voids and cavities throughout the material. This porous morphology, marked by irregular shapes and uneven surfaces, is characteristic of ACs and is key to its high surface area [71]. Furthermore, the edges of the particles are less defined, reflecting the partial breakdown of the stacked layer structure observed in the original graphite. Overall, the results indicate that KOH activation of recovered graphite simultaneously preserves the graphitic structure while introducing structural imperfections that contribute to porosity development. This can be attributed to selective etching, where ordered graphitic domains remain intact, while defects such as vacancies are introduced at the edges, grain boundaries, or amorphous regions. Similar observations were reported by Tai et al. [72], who found that increasing KOH concentrations led to surface roughening, particle fragmentation, and enhanced K^+ ions transmission, while XRD confirmed the retention of characteristic graphite peaks.

To examine the interaction of potassium species with the carbon

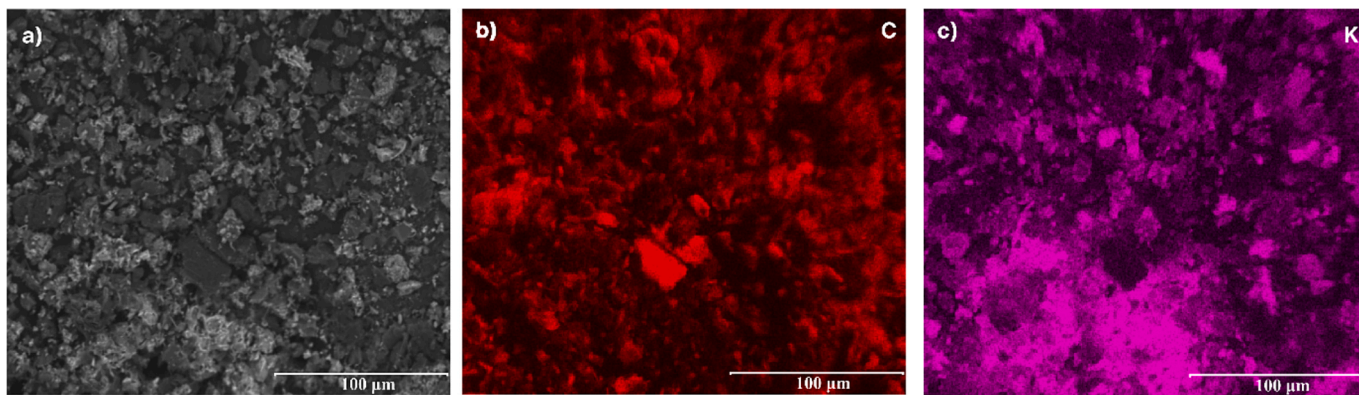


Fig. 11. EDS analysis of the unwashed, recovered graphite-based AC sample (AC-800_1:6): (a) representative SEM micrograph and corresponding elemental intensity maps for (b) C and (c) K.

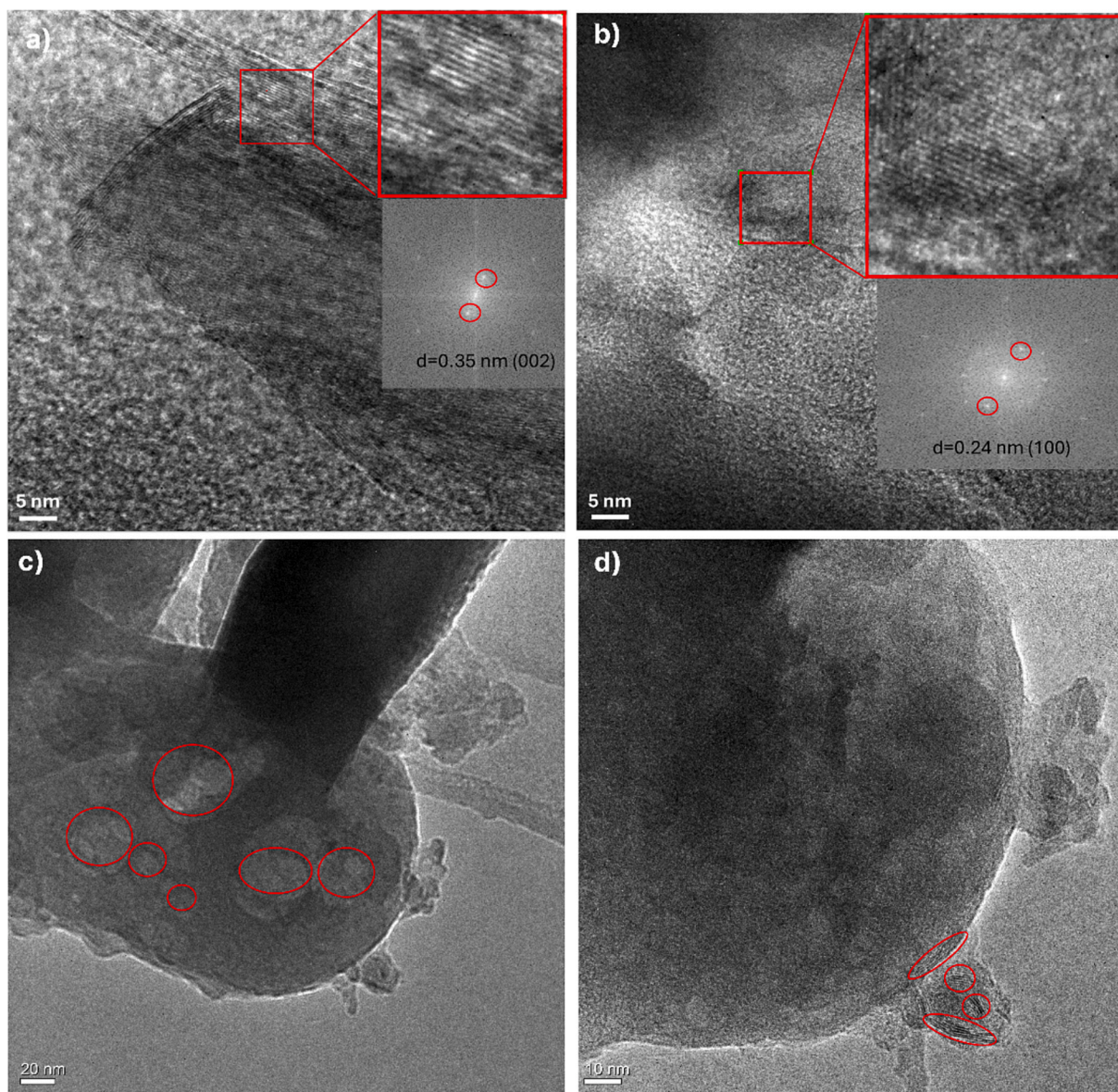


Fig. 12. HRTEM images and FFT patterns of recovered graphite (a) and AC-800_1:6 (b), and TEM images of AC-800_1:6 showing (c) mesopore-like voids formation and (d) structural defects with partially delaminated graphitic layers at the particle edge.

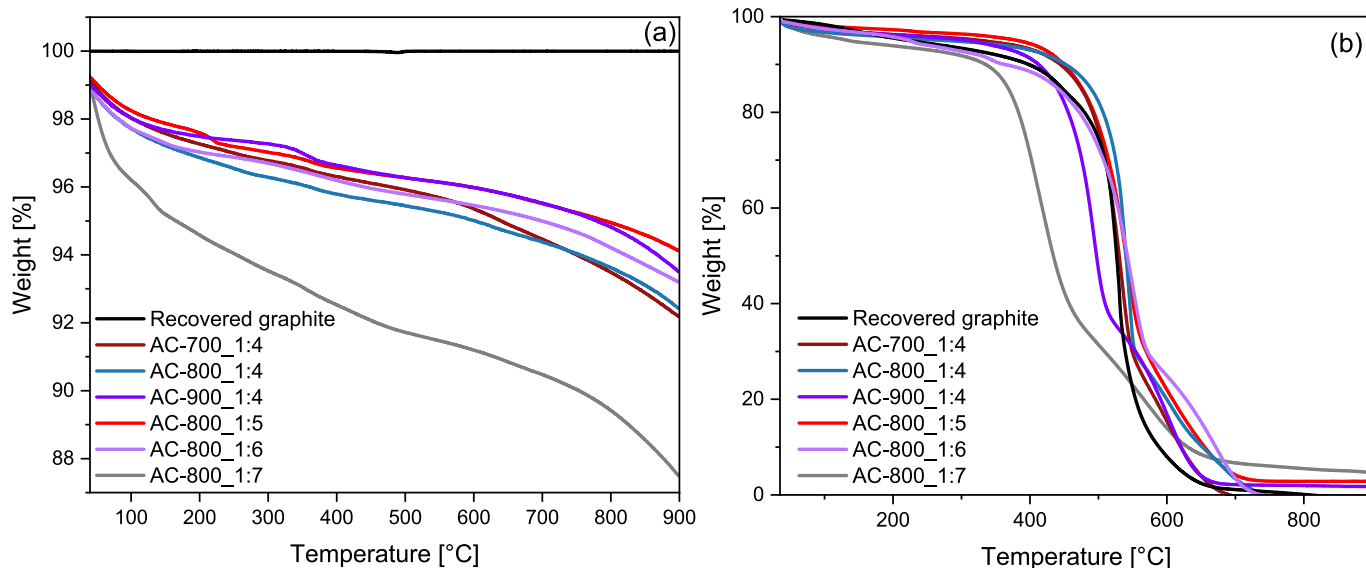


Fig. 13. TGA curves of the samples subjected to a heating rate of 10 K/min from 30 to 900 °C: (a) in a nitrogen atmosphere; (b) in an air atmosphere for activated carbon samples synthesized at different temperatures and graphite:KOH ratios.

matrix of recovered graphite during high-temperature KOH activation, and the retention of potassium-rich compounds, EDS analysis of the unwashed sample is presented in Fig. 11. C mapping shows a relatively uniform distribution, consistent with the graphitic structure of the material. In contrast, K mapping reveals a non-uniform distribution, with localized regions exhibiting high potassium concentrations (13.3 wt%). This uneven distribution arises from the retention of K-containing compounds, such as KHCO_3 , K_2CO_3 , and K_2O , formed during thermochemical conversion at 800 °C, along with other volatile by-products [73]. The localized potassium-rich regions likely result from the agglomeration or incomplete dispersion of these K species, contributing to the observed inhomogeneity [32].

To gain deeper insight into the microstructural differences between the recovered graphite and AC-800_1:6, HRTEM combined with FFT analysis was performed. Fig. 12 shows representative HRTEM images and the corresponding FFT patterns for both samples. The recovered graphite (Fig. 12(a)) presents well-ordered and extended lattice fringes, with an interlayer distance of approximately 0.35 nm. This spacing corresponds to the (002) planes of graphitic carbon and is slightly larger than the ideal value (0.335 nm) obtained from XRD analysis, which can be attributed to minor turbostratic disorder. The sharp and symmetric reflections observed in the FFT pattern confirm the presence of long-range stacking along the c-axis, characteristic of layered graphite [74,75]. In contrast, the AC-800_1:6 (Fig. 12(b)) exhibits a significantly more disordered microstructure. The HRTEM image reveals no evidence of long-range stacking, but short, curved fringes can still be observed locally. The dominant lattice spacing in this region is approximately 0.24 nm, which aligns with the (100) in-plane lattice of hexagonal carbon, rather than the interlayer (002) spacing. The FFT pattern is diffuse and lacks the symmetry seen in the recovered graphite sample, indicating that structural coherence is lost during activation [76]. This localized disruption of (002) stacking is further supported by XRD analysis, which reveals broadening and reduced intensity of the (002) peak, along with a moderate decrease in L_c . However, the presence of (100) lattice fringes in the TEM-FFT, together with the stable d_{002} and high L_a values from XRD, confirms that while vertical order is partially degraded, the planar graphitic structure and in-plane crystallinity are largely preserved (Table 2). This disruption of graphitic stacking is consistent with KOH activation pathways involving selective removal of less ordered carbon and partial gasification of graphene layers. These processes fragment the structure into nanoscale domains with edge

defects, promoting porosity [77]. As shown in Fig. 12(c), circular low-contrast features within the carbon matrix suggest the formation of mesopore-like voids, while Fig. 12(d) shows structural defects and partially delaminated graphitic layers at the particle edge, indicating a disordered framework consistent with hierarchical porosity, including regions near the surface. Combined with BET surface area and porosity data, the observed loss of (002) features alongside preserved in-plane order confirms a transition to a defect-rich carbon network. This direct structural evidence supports the view that KOH activation not only increases disorder, but specifically disrupts interlayer stacking, forming short-range graphene-like domains with enhanced surface accessibility.

3.4. Thermal performance of recovered graphite-based ACs in inert and oxidative conditions

The TGA curves, illustrating the thermal stability and decomposition behavior of the samples under a N_2 atmosphere up to 900 °C, are presented in Fig. 13(a). Recovered graphite exhibited minimal weight loss (<0.5 % wt.) throughout the entire temperature range, reflecting its high thermal stability and crystalline structure. ACs demonstrated a generally similar shape across all activation temperatures and KOH-to-graphite mass ratios. This similarity indicates comparable thermal events, such as moisture release, decomposition of oxygen-containing functional groups (OCFGs) and structural degradation, occurring in distinct temperature regions [78]. Despite the uniformity in curve shape, the extent of weight loss varies depending on the activation temperature and chemical ratio, reflecting differences in structural integrity and OCFGs. ACs prepared at activation temperatures of 700 °C, 800 °C, and 900 °C showed an initial weight loss below 200 °C, consistent across all samples (~2–3 wt%), that can be attributed to the removal of water, physisorbed or adsorbed volatiles [79]. Between 200 °C and 600 °C, the most pronounced decomposition was observed for AC-800 (~5 wt%), indicating the highest concentration of oxygen-containing functional groups, which degrade at intermediate temperatures [80]. However, above 600 °C, AC-700_1:4 exhibited the greatest weight loss (~8% wt.), which may indicate a higher proportion of thermally less stable components within the carbon framework. Among ACs synthesized with graphite-to-KOH ratios of 1:5, 1:6, and 1:7, the AC-800_1:5 and AC-800_1:6 demonstrated moderate thermal stability, with approximately 6 wt% and 7 wt% loss by 900 °C, suggesting stable porous structure. The

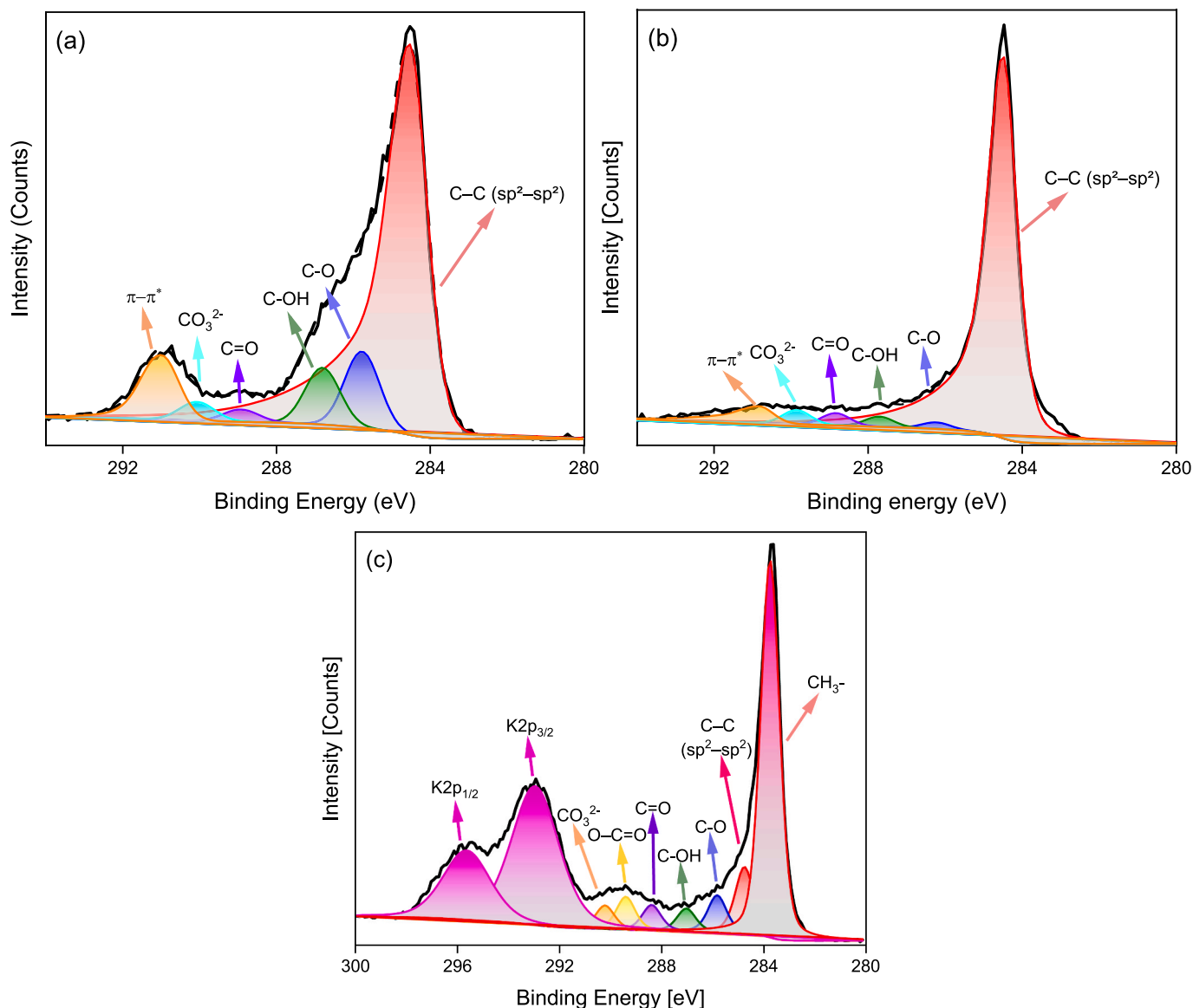


Fig. 14. XPS spectra in the C1s region for (a) recovered graphite, (b) the recovered graphite-based AC sample (AC-800_1:6), and in the C1s-K2p region for (c) unwashed AC-800_1:6.

AC-800_1:7 showed the lowest stability (~ 13 wt%), likely resulting from excessive activation, which may have caused structural densification or potential pore collapse, as observed previously, despite the higher chemical loading. Notably, the overall standard deviation was very low, around 0.5 %, indicating consistent results across measurements.

The weight change observed during the oxidation of the samples in an air atmosphere is illustrated in the TGA curves shown in Fig. 13(b). A general trend in thermal degradation is observed, characterized by an initial gradual change in sample weight, followed by a sharp decline as the temperature rises [81]. Weight loss initiates around 450 °C for most materials, marking the onset of carbon structure oxidation. It intensifies significantly between 500 °C and 650 °C, signifying the full oxidation of the more resilient carbon frameworks. The rate and onset of degradation seems to vary depending on the activation conditions, with some samples exhibiting a more gradual weight loss, while others degrading more rapidly. Among the ACs, the AC-800_1:7 has a weight loss that begins earlier, at approximately 350 °C, and accelerates rapidly above 400 °C. The activation conditions for AC-800_1:7 appear to have resulted in a framework that lacks the robust 3D carbon network characteristic of graphite. This network, composed of numerous graphene-stacked layers

held together by van der Waals forces, is known for providing exceptional stability under oxidative conditions [82]. As a result, the AC-800_1:7 material may exhibit fewer thermally resistant carbon bonds or an alternative structural configuration, which could influence its stability compared to other ACs.

3.5. Surface chemistry and carbon framework evolution through KOH activation

Fig. 14(a, b) illustrates the C1s spectra for the recovered graphite and the AC-800_1:6 after the KOH treatment, respectively. The asymmetric C1s peaks at a binding energy of 284.6 eV, coupled with a π - π^* shake-up at approximately 291.0 eV, are the characteristic features of sp^2 -hybridized carbon, confirming the graphitic nature of the samples. This graphitic carbon is the dominant chemical state in both samples [83]. Besides that, the other oxidized states including C-O (285.8 eV), C-OH (287.0 eV), C=O (288.8 eV), and CO_3^{2-} (290.0 eV) are determined. After KOH activation, the intensity of the graphitic carbon (C-C, sp^2 - sp^2) peak increases, reflecting graphitization or the development of a more ordered graphitic structure. However, K intercalation during activation

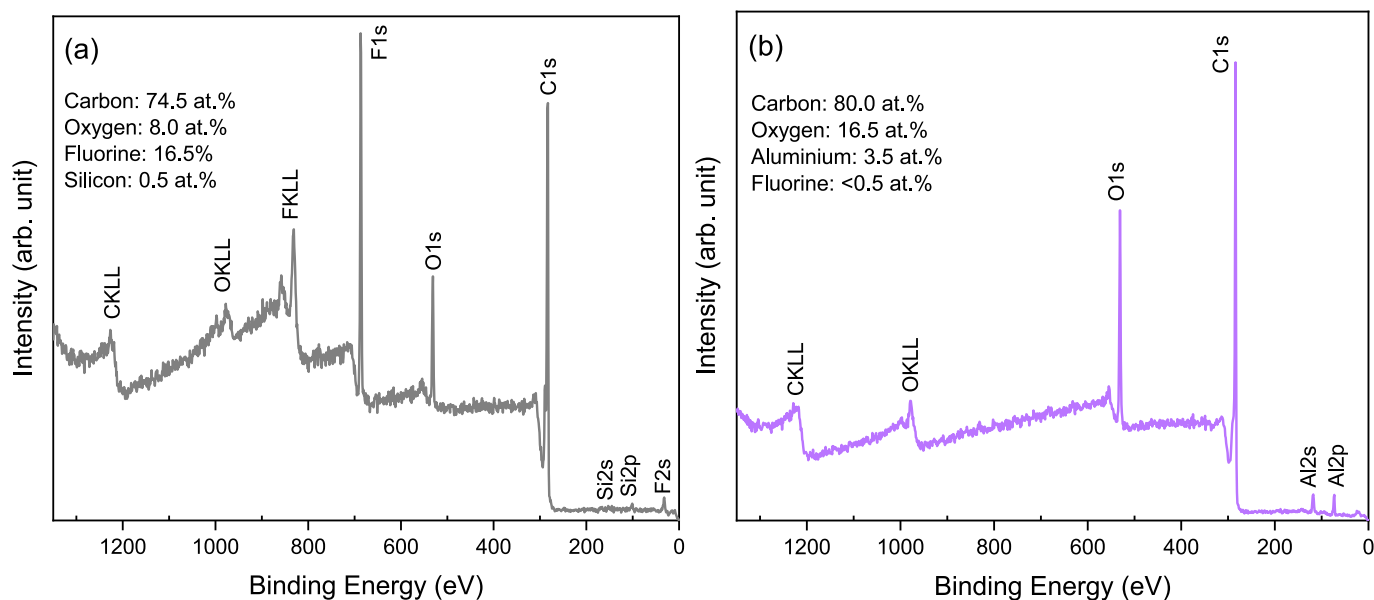


Fig. 15. Survey spectra of (a) recovered graphite, and (b) recovered graphite-based AC sample (AC-800_1:6).

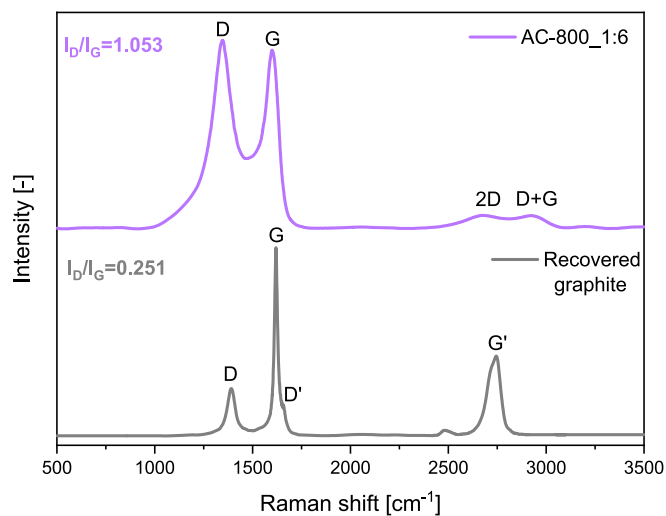


Fig. 16. Raman spectra of the recovered graphite and recovered graphite-based AC sample (AC-800_1:6).

can also cause local structural distortions, as confirmed later by Raman spectroscopy, which shows some disorder alongside the overall graphitization trend. Simultaneously, the oxidized states decrease non-uniformly, potentially due to high-temperature reactions with KOH that remove pre-existing OCFGs from the surface. This process may also involve redox reactions, where metallic potassium, formed during activation at temperatures above 762 °C, interacts with surface oxygen groups, altering their arrangement and promoting their removal [84,85].

In Fig. 14(c), the XPS spectrum in the C1s–K2p region of unwashed AC-800_1:6 reveals both C–C (sp^2 – sp^2) and CH_3 -related peaks. While the sp^2 – sp^2 bonding is consistent with the expected graphitic structure, the appearance of CH_3 -associated signals is atypical, which is likely due to surface contamination, residual potassium compounds, or hydrocarbon fragments introduced during activation or handling. Additionally, the presence of the O–C=O group (289.2 eV) suggests carbonate-like phases formed via surface oxidation or interactions with residual potassium-containing compounds, as confirmed by XRD analysis. The $K2p_{3/2}$ and $K2p_{1/2}$ peaks further support the presence of these K-based species,

which may influence the local carbon bonding environment.

In view of the quantitative analysis of the surface composition via survey scan (Fig. 15), the overall carbon content increases from 74.5 at.% in the recovered graphite to 80.0 at.% after activation. This increase is attributed to the removal of surface contaminants, including fluorine, which decreases significantly from 16.5 at.% to below 0.5 at.%, thereby enriching the surface carbon proportion. Conversely, the oxygen content rises from 8.0 at.% to 16.5 at.% due to the introduction of OCFGs during the KOH activation process, consistent with expected surface oxidation. However, high-resolution C1s spectra shows a reduction in the intensities of oxidized carbon states after activation (Fig. 14). This apparent contradiction most probably arises from the redistribution or transformation of oxygen-containing species [86]. While specific oxidized carbon states decrease, the overall oxygen content likely increases due to the formation of other OCFGs. These groups are not directly detected in the C1s spectra but contribute to the higher oxygen signal in the survey scan without significantly influencing the C1s peaks. Finally, aluminium (~9.0 at.% Al_2O_3) that observed in the sample originates from the alumina crucible used during the thermochemical process. To facilitate clearer interpretation, the XPS analysis results are summarized in comparative form in Table S4.

The Raman spectra of the recovered graphite and the AC-800_1:6 (Fig. 16) provide insight into the structural changes induced by KOH activation, complementing the observations from the XPS analysis. In Raman spectroscopy, the D mode corresponds to the breathing modes of sp^2 atoms in rings and is indicative of defects or disorder in the carbon structure, while the G mode arises from the in-plane vibration of sp^2 -bonded carbon atoms, representing the graphitic domains. The intensity ratio I_D/I_G , derived from the integrated areas under the D and G peaks, serves as a measure of structural disorder. For the recovered graphite sample, the I_D/I_G ratio is 0.251, indicating a low level of structural disorder and a relatively high graphitic content. After activation, this ratio increases significantly to 1.053, reflecting the introduction of defects and greater disorder in the carbon structure [87]. These structural modifications, such as edge sites and functionalized pores, are likely a result of KOH etching and are consistent with the higher defect density observed in the Raman spectroscopy analysis. At the same time, the XPS spectra at the C1s regions (Fig. 14) reveal a notable increase in the relative intensity of the sp^2 -hybridized carbon peak in the AC-800_1:6, suggesting enhanced graphitization at the surface level, likely due to the removal of oxidized states during activation [88]. Together, the

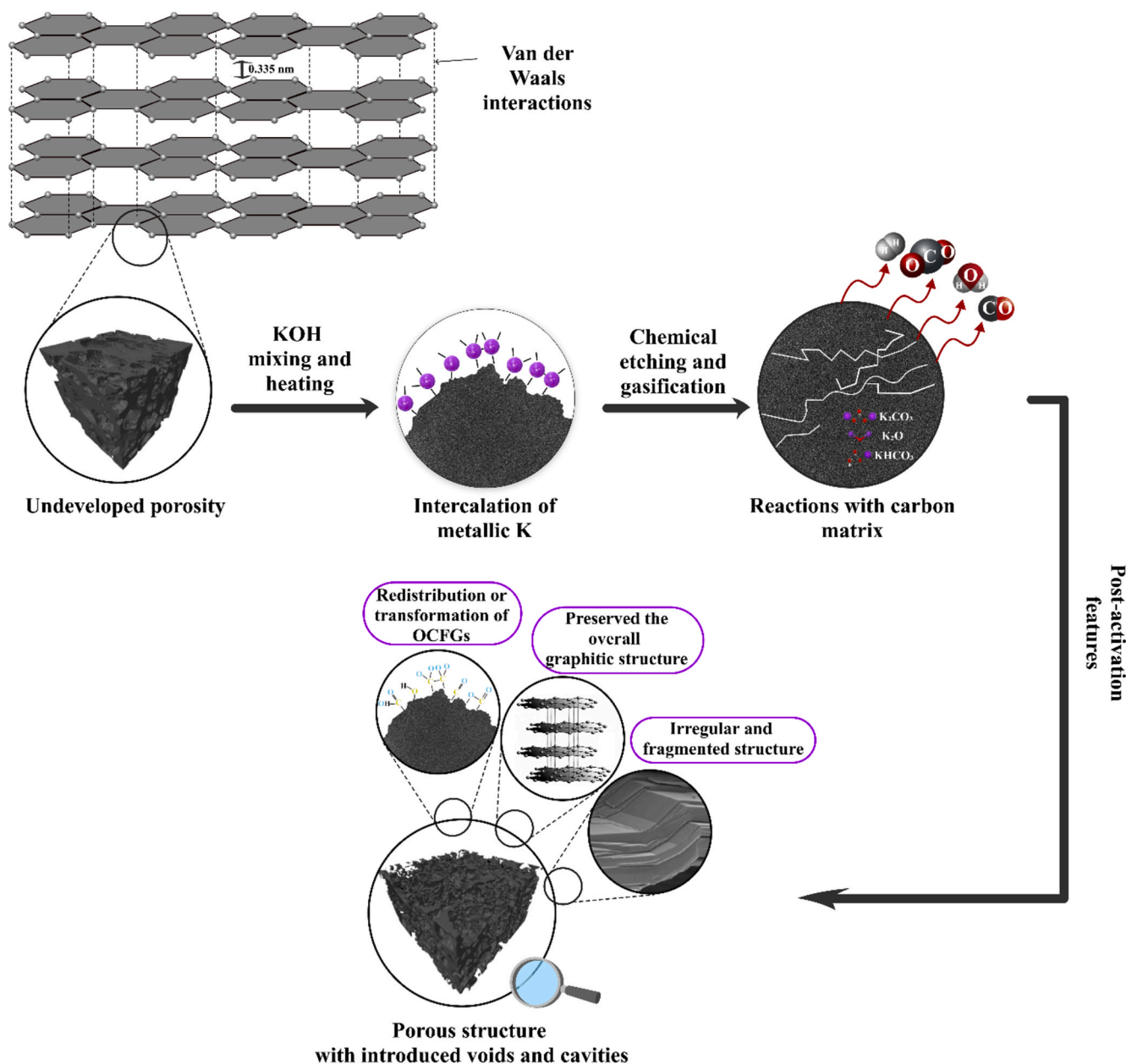


Fig. 17. Mechanistic pathway of KOH activation for converting unused hazardous graphite from NMC 111 into ACs.

Raman and XPS spectroscopic analyses highlight a complex interplay: while Raman spectroscopy indicates increased disorder within the carbon lattice, XPS reveals improved structural ordering in the surface carbon domains.

4. Conclusions

This study provides a comprehensive assessment of the transformation of graphite recovered from NMC 111 black mass of spent lithium-ion batteries into activated carbons via KOH activation (Fig. 17). The findings explore the changes in the textural, structural, morphological, and surface chemistry properties of the material throughout the KOH activation process.

KOH activation involves the selective removal of carbon from recovered graphite, leading to defect formation, disorder, and pore development, resulting in a microporous and mesoporous structure. Tailored activation conditions (800 °C, 1:6 graphite-to-KOH ratio) yielded ACs with a specific surface area of 678 m²/g, a total pore volume

of 0.442 cm³/g, and a balanced micropore (53 %) and mesopore (47 %) distribution, contributing to the material's hierarchical porosity. Structural analysis confirmed the preservation of the graphitic framework. XRD revealed characteristic crystallographic planes, including (002), (100), (101), (104), (110), and (112), with an unchanged interlayer spacing of 0.335 nm. However, the broadening and reduction in intensity of the (002) peak indicated that activation predominantly affected the less ordered regions, leading to some loss of long-range order in the graphitic structure. The increased I_D/I_G ratio (0.251 to 1.053) in Raman spectroscopy indicated enhanced defect density and disorder.

SEM revealed a transition from smooth graphite layers to a fragmented, rough surface, while TEM showed a complex nanoscale architecture with mesopore-like voids and structural defects at the particle edge. FFT analysis of the recovered graphite showed well-ordered lattice fringes with an interlayer distance of ~0.35 nm, corresponding to the (002) planes. This spacing, slightly larger than the ideal 0.335 nm from XRD, suggests minor turbostratic disorder. In contrast, FFT of the AC

revealed a dominant lattice spacing of ~ 0.24 nm, highlighting the exposure of the (1 0 0) in-plane lattice and disruption of the interlayer stacking.

EDS mapping confirmed a predominantly carbon-rich composition with localized potassium residues. XPS analysis identified oxygen-containing functional groups (C–O, C–OH, C=O, and CO_3^{2-}), contributing to chemical reactivity. Thermal stability tests demonstrated high stability under inert conditions and increased reactivity in oxidative environments, reflecting structural defects and oxygen functionalities introduced during activation.

These results underscore the potential of chemical activation for converting unused hazardous graphite waste from NMC 111 into functional materials for applications such as CO_2 capture, gas separation, energy storage, water treatment, and catalysis. Future research should evaluate the application-specific performance of these ACs in industrial gas sorption systems and energy storage devices. Expanding the methodology to diverse black mass compositions and LiB chemistries will enhance scalability. Additionally, optimizing energy efficiency, reducing chemical consumption, and conducting life cycle assessments will be crucial for industrial adoption. To further highlight the benefits of the strong alkali-assisted process, comparative studies with commercial graphite and activated carbons are recommended to emphasize the unique characteristics and performance advantages of the recycled graphite-derived porous carbon from LiBs.

CRedit authorship contribution statement

Bartosz Dziejarski: Writing – original draft, Visualization, Validation, Software, Methodology, Investigation, Formal analysis, Data curation, Conceptualization, Writing – review & editing. **Jose Eduardo Arevalo Fester:** Formal analysis, Data curation, Conceptualization, Writing – review & editing. **Jarosław Serafin:** Validation, Investigation, Formal analysis, Conceptualization, Data curation, Software, Writing – review & editing, Methodology. **Martina Petranikova:** Writing – original draft, Supervision, Resources, Investigation, Funding acquisition, Conceptualization. **Eric Tam:** Writing – original draft, Validation, Software, Investigation, Formal analysis, Data curation. **Anna Martinnelli:** Validation, Supervision, Software, Resources, Investigation, Formal analysis. **Renata Krzyżyńska:** Supervision, Investigation. **Klas Andersson:** Supervision, Methodology, Investigation, Conceptualization. **Pavleta Knutsson:** Supervision, Resources, Project administration, Methodology, Investigation, Funding acquisition, Formal analysis, Conceptualization.

Declaration of competing interest

The authors declare that they have no known competing financial interests or personal relationships that could have appeared to influence the work reported in this paper. This work was supported by the Swedish Energy Agency (Project Nos. P2021-90022 and P2023-00146).

Appendix A. Supplementary data

Supplementary data to this article can be found online at <https://doi.org/10.1016/j.matdes.2025.114073>.

Data availability

Data will be made available on request.

References

- [1] M. Slattery, J. Dunn, A. Kendall, Transportation of electric vehicle lithium-ion batteries at end-of-life: a literature review, *Resour. Conserv. Recycl.* 174 (2021) 105755.
- [2] C.D. Quilty, D. Wu, W. Li, D.C. Bock, L. Wang, L.M. Housel, E.S. Takeuchi, Electron and ion transport in lithium and lithium-ion battery negative and positive composite electrodes, *Chem. Rev.* 123 (4) (2023) 1327–1363.
- [3] X. Zhang, Z. Li, L. Luo, Y. Fan, Z. Du, A review on thermal management of lithium-ion batteries for electric vehicles, *Energy* 238 (2022) 121652, <https://doi.org/10.1016/j.energy.2021.121652>.
- [4] IEA (2024), Global EV Outlook 2024, IEA, Paris <https://www.iea.org/reports/global-ev-outlook-2024>, Licence: CC BY 4.0.
- [5] J. Jayaprakash, J.A. Kumar, J. Parthipan, A. Karthikeyan, M. Anish, N. Joy, Review on hybrid electro chemical energy storage techniques for electrical vehicles: technical insights on design, performance, energy management, operating issues & challenges, *J. Storage Mater.* 72 (2023) 108689.
- [6] M.M. Rana, M. Uddin, M.R. Sarkar, S.T. Meraj, G.M. Shafiqullah, S.M. Mueen, T. Jamal, Applications of energy storage systems in power grids with and without renewable energy integration—A comprehensive review, *J. Storage Mater.* 68 (2023) 107811.
- [7] W. Wang, B. Yuan, Q. Sun, R. Wennersten, Application of energy storage in integrated energy systems—A solution to fluctuation and uncertainty of renewable energy, *J. Storage Mater.* 52 (2022) 104812.
- [8] S.B. Wali, M.A. Hannan, P.J. Ker, S.A. Rahman, K.N. Le, R.A. Begum, T.I. Mahlia, Grid-connected lithium-ion battery energy storage system towards sustainable energy: a patent landscape analysis and technology updates, *J. Storage Mater.* 77 (2024) 109986.
- [9] J. Fleischmann, M. Hanicke, E. Horetsky, D. Ibrahim, S. Jautelat, M. Linder, ... A. van de Rijt, *Battery 2030: Resilient, sustainable, and circular*. McKinsey & Company, 2-18. 2023. <https://www.mckinsey.com/industries/automotive-and-assembly/our-insights/battery-2030-resilient-sustainable-and-circular/>.
- [10] X. Gu, H. Bai, X. Cui, J. Zhu, W. Zhuang, Z. Li, Z. Song, Challenges and opportunities for second-life batteries: key technologies and economy, *Renew. Sustain. Energy Rev.* 192 (2024) 114191.
- [11] V. Srivastava, V. Rantala, P. Mehdipour, T. Kauppinen, S. Tuomikoski, A. Heponiemi, U. Lassi, A comprehensive review of the reclamation of resources from spent lithium-ion batteries, *Chem. Eng. J.* (2023) 145822.
- [12] B. Niu, Z. Xu, J. Xiao, Y. Qin, Recycling hazardous and valuable electrolyte in spent lithium-ion batteries: urgency, progress, challenge, and viable approach, *Chem. Rev.* 123 (13) (2023) 8718–8735.
- [13] B. Niu, J. Xiao, Z. Xu, Utilizing spent Li-ion batteries to regulate the π -conjugated structure of gC_3N_4 : a win-win approach for waste recycling and highly active photocatalyst construction, *J. Mater. Chem. A* 9 (1) (2021) 472–481.
- [14] X. Zhang, L. Li, E. Fan, Q. Xue, Y. Bian, F. Wu, R. Chen, Toward sustainable and systematic recycling of spent rechargeable batteries, *Chem. Soc. Rev.* 47 (19) (2018) 7239–7302.
- [15] K. Elong, M.F. Kasim, A. Azahidi, Z. Osman, LiNi_{0.3}Mn_{0.3}Co_{0.3}O₂(NMC 111) cathode material synthesized via combustion method: effect of combustion fuel on structure, morphology and their electrochemical performances, *Mater. Today Proc.* (2023).
- [16] F.N.U. Khan, M.G. Rasul, A.S.M. Sayem, N. Mandal, Maximizing energy density of lithium-ion batteries for electric vehicles: a critical review, *Energy Rep.* 9 (2023) 11–21.
- [17] E. Katanaki, A. Giannis, Dynamic estimation of end-of-life electric vehicle batteries in the EU-27 considering reuse, remanufacturing and recycling options, *J. Clean. Prod.* 393 (2023) 136349.
- [18] A. Tankou, G. Bieker, D. Hall, February). Scaling up reuse and recycling of electric vehicle batteries: Assessing challenges and policy approaches, in: *In Proc. ICCT, 2023*, pp. 1–138.
- [19] A.M. Abdalla, M.F. Abdullah, M.K. Dawood, B. Wei, Y. Subramanian, A.T. Azad, A. K. Azad, Innovative lithium-ion battery recycling: sustainable process for recovery of critical materials from lithium-ion batteries, *J. Storage Mater.* 67 (2023) 107551.
- [20] Y. Zou, A. Chernyaev, M. Ossama, S. Seisko, M. Lundström, Leaching of NMC industrial black mass in the presence of LFP, *Sci. Rep.* 14 (1) (2024) 10818.
- [21] M. Olutogun, A. Vanderbruggen, C. Frey, M. Rudolph, D. Bresser, S. Passerini, Recycled graphite for more sustainable lithium-ion batteries, *Carbon Energy* e483 (2024).
- [22] S. Natarajan, V. Aravindan, An urgent call to spent LIB recycling: whys and wherefores for graphite recovery, *Adv. Energy Mater.* 10 (37) (2020) 2002238.
- [23] K. Bilisik, M. Akter, Polymer nanocomposites based on graphite nanoplatelets (GNPs): a review on thermal-electrical conductivity, mechanical and barrier properties, *J. Mater. Sci.* 57 (15) (2022) 7425–7480.
- [24] Y.A. Kumar, J.K. Alagarasan, T. Ramachandran, M.D. Rezek, M.A. Bajaber, A. A. Alalwiat, M. Lee, The landscape of energy storage: insights into carbon electrode materials and future directions, *J. Storage Mater.* 86 (2024) 111119.
- [25] K. Yang, Z. Ling, X. Fang, Z. Zhang, Introducing a flexible insulation network to the expanded graphite-based composite phase change material to enhance dielectric and mechanical properties for battery thermal management, *J. Storage Mater.* 66 (2023) 107486.
- [26] I.K. Tetteh, I. Issahaku, A.Y. Tetteh, Recent advances in synthesis, characterization, and environmental applications of activated carbons and other carbon derivatives, *Carbon Trends* (2024) 100328.
- [27] F. Nawaz, M. Ali, S. Ahmad, Y. Yong, S. Rahman, M. Naseem, N. Ali, Carbon based nanocomposites, surface functionalization as a promising material for VOCs (volatile organic compounds) treatment, *Chemosphere* (2024) 143014.
- [28] L.A. Xing, F. Yang, X. Zhong, Y. Liu, H. Lu, Z. Guo, J. Pan, Ultra-microporous cotton fiber-derived activated carbon by a facile one-step chemical activation strategy for efficient CO_2 adsorption, *Sep. Purif. Technol.* 324 (2023) 124470.

- [29] C. Madhusha, T. Jayasundara, I. Munaweera, C. Perera, G. Wijesinghe, M. Weerasekera, N. Kottegoda, Synthesis and structural characterization of copper nanoparticles doped activated carbon derived from coconut coir for drinking water purification, *Mater. Today Chem.* 27 (2023) 101312.
- [30] S. Mandal, J. Hu, S.Q. Shi, A comprehensive review of hybrid supercapacitor from transition metal and industrial crop based activated carbon for energy storage applications, *Mater. Today Commun.* 34 (2023) 105207.
- [31] J.H. Wee, S. Shin, D.W. Kim, C. Lee, Y.A. Kim, M.W. Shin, S.Y. Yeo, Boron-doped activated carbon supports for cobalt-catalyzed oxygen evolution in alkaline electrolyte, *ACS Appl. Mater. Interfaces* 15 (15) (2023) 18771–18780.
- [32] B. Dziejarski, R. Faust, J. Serafin, R. Krzyżyńska, K. Andersson, P. Knutsson, Insights into activation pathways of recovered carbon black (rCB) from end-of-life tires (ELTs) by potassium-containing agents, *ACS Omega* 9 (29) (2024) 31814–31831.
- [33] G. Singh, A.M. Ruban, X. Geng, A. Vinu, Recognizing the potential of K-salts, apart from KOH, for generating porous carbons using chemical activation, *Chem. Eng. J.* 451 (2023) 139045.
- [34] J. Singh, H. Bhunia, S. Basu, Adsorption of CO₂ on KOH activated carbon adsorbents: effect of different mass ratios, *J. Environ. Manage.* 250 (2019) 109457.
- [35] M. Gayathiri, T. Pulingam, K.T. Lee, K. Sudesh, Activated carbon from biomass waste precursors: factors affecting production and adsorption mechanism, *Chemosphere* 294 (2022) 133764.
- [36] M.M. Amin, L.S. Mohamed, M.M. Hossain, S.A. Razzak, M.N. Siddiquee, Prospects and challenges of carbon fiber production from heavy petroleum fractions, *Ind. Eng. Chem. Res.* 63 (36) (2024) 15613–15636.
- [37] I. Skoczko, R. Guminski, Tests on the application of various types of biomass for activated carbon production, *J. Ecol. Eng.* 25 (1) (2024).
- [38] M. Tesfaye Gari, B. Tessema Asfaw, S.K. Arumugasamy, L. Deso Abo, M. Jayakumar, Natural resources-based activated carbon synthesis, in: *Encyclopedia of Green Materials*, Springer Nature Singapore, Singapore, 2024, pp. 1520–1530.
- [39] Z. Shang, W. Yu, J. Zhou, X. Zhou, Z. Zeng, R. Tursun, S. Xu, Recycling of spent lithium-ion batteries in view of graphite recovery: a review, *ETransportation* (2024) 100320.
- [40] L.Y. Meng, S.J. Park, Effect of heat treatment on CO₂ adsorption of KOH-activated graphite nanofibers, *J. Colloid Interface Sci.* 352 (2) (2010) 498–503.
- [41] H. Yuan, L.Y. Meng, S.J. Park, KOH-activated graphite nanofibers as CO₂ adsorbents, *Carbon Lett.* 19 (1) (2016) 99–103.
- [42] J. Rouquerol, G.V. Baron, R. Denoyel, H. Giesche, J. Groen, P. Klobes, K. Unger, The characterization of macroporous solids: an overview of the methodology, *Microporous Mesoporous Mater.* 154 (2012) 2–6.
- [43] J. Serafin, M. Ouzzine, O.F. Cruz Jr, J. Sreńscek-Nazzal, I.C. Gómez, F.Z. Azar, C. R. Rambo, Conversion of fruit waste-derived biomass to highly microporous activated carbon for enhanced CO₂ capture, *Waste Manag.* 136 (2021) 273–282.
- [44] K.R. Hallam, J.E. Darnbrough, C. Paraskevoulakos, P.J. Heard, T.J. Marrow, P. E. Flewitt, Measurements by x-ray diffraction of the temperature dependence of lattice parameter and crystallite size for isostatically-pressed graphite, *Carbon Trends* 4 (2021) 100071.
- [45] P. Puech, M. Jeanningros, D. Neumeyer, M. Monthieux, Addressing the effect of stacking faults in X-ray diffractograms of graphite through atom-scale simulations, *Carbon Trends* 13 (2023) 100311.
- [46] F.T.L. Muniz, M.R. Miranda, C. Morilla dos Santos, J.M. Sasaki, The Scherrer equation and the dynamical theory of X-ray diffraction, *Found. Crystallogr.* 72 (3) (2016) 385–390.
- [47] S. Basak, R. Das, Confirmation of the presence of edge dislocations in the prepared FCC ZnTe nanocrystals from the study of structural analysis through the MWH method with added Fourier analysis (WA method) of diffraction peaks, *Mater. Sci. Semicond. Process.* 179 (2024) 108477.
- [48] R. Sharma, D.P. Bisen, U. Shukla, B.G. Sharma, X-ray diffraction: a powerful method of characterizing nanomaterials, *Recent Res. Sci. Technol.* 4 (8) (2012) 77–79.
- [49] V. Kumar, A. Kumar, D.J. Lee, S.S. Park, Estimation of number of graphene layers using different methods: a focused review, *Materials* 14 (16) (2021) 4590.
- [50] S. Shimizu, N. Matubayasi, Understanding sorption mechanisms directly from isotherms, *Langmuir* 39 (17) (2023) 6113–6125.
- [51] V.G. Baldovino-Medrano, V. Niño-Celis, R. Isaacs Giraldo, Systematic analysis of the nitrogen adsorption-desorption isotherms recorded for a series of materials based on microporous-mesoporous amorphous aluminosilicates using classical methods, *J. Chem. Eng. Data* 68 (9) (2023) 2512–2528.
- [52] G. Chen, Z. Liu, G. Yang, Q. Zhang, T. Lan, C. Zhang, S. He, Synthesis of chain-like nitrogen-doped carbon for high-performance supercapacitors, *Colloids Surf. A Physicochem. Eng. Asp.* 687 (2024) 133498.
- [53] Z. Song, J. Zhang, S. Jin, C. Liu, A. Abula, J. Hou, L. Ma, The occurrences and mobility of shale oil in the pore space of terrestrial shale, *Fuel* 374 (2024) 132377.
- [54] T. Manimekala, R. Sivasubramanian, M.A. Dar, G. Dharmalingam, Crafting the architecture of biomass-derived activated carbon via electrochemical insights for supercapacitors: a review, *RSC Adv.* 15 (4) (2025) 2490–2522.
- [55] N. Boonraksa, E. Swatsitang, K. Wongsaprom, Electrochemical performance of KOH-activated lotus seedpods carbon, *Mater. Sci. Eng. B* 301 (2024) 117151.
- [56] T. Ji, X. Liu, T. Zhang, Y. Shi, D. Sheng, H. Yin, D. Chao, Potassium metal underpotential deposition in crystalline carbon of potassium-ion batteries, *Adv. Energy Mater.* 14 (40) (2024) 2401908.
- [57] G. Wang, Yu. Minghao, X. Feng, Carbon materials for ion-intercalation involved rechargeable battery technologies, *Chem. Soc. Rev.* 50 (4) (2021) 2388–2443.
- [58] A.A. Papaderakis, A. Ejigu, J. Yang, A. Elgendy, B. Radha, A. Keerthi, R.A. Dryfe, Anion intercalation into graphite drives surface wetting, *J. Am. Chem. Soc.* 145 (14) (2023) 8007–8020.
- [59] R. Yang, L. Mei, Z. Lin, Y. Fan, J. Lim, J. Guo, Z. Zeng, Intercalation in 2D materials and in situ studies, *Nat. Rev. Chem.* (2024) 1–23.
- [60] Y. Luo, Q. Jiang, J. Liu, H. Yang, X. Liao, F. Huang, J. He, Mesoporous collapsing encapsulated carbon dots: direct evidence for the effect of multiple-confined interactions of silica on efficient long-lived phosphorescence, *Chem. Eng. J.* 486 (2024) 150436.
- [61] T. Yin, Z. Zhang, L. Xu, C. Li, D. Han, Preparation of green high-performance biomass-derived hard carbon materials from bamboo powder waste, *ChemistryOpen* 13 (5) (2024) e202300178.
- [62] J. Serafin, M. Baca, M. Biegun, E. Mijowska, R.J. Kalenciuk, J. Sreńscek-Nazzal, B. Michalkiewicz, Direct conversion of biomass to nanoporous activated biocarbons for high CO₂ adsorption and supercapacitor applications, *Appl. Surf. Sci.* 497 (2019) 143722.
- [63] J. Kafle, J. Harris, J. Chang, J. Koshina, D. Boone, D. Qu, Development of wide temperature electrolyte for graphite/LiNiMnCoO₂ Li-ion cells: high throughput screening, *J. Power Sources* 392 (2018) 60–68.
- [64] H. Zhang, Y. Yang, D. Ren, L. Wang, X. He, Graphite as anode materials: fundamental mechanism, recent progress and advances, *Energy Storage Mater.* 36 (2021) 147–170.
- [65] D. Kaiser, S. Pavón, M. Bertau, Recovery of Al, Co, Cu, Fe, Mn, and Ni from Spent LIBs after Li selective separation by the COOL-Process. Part 1: leaching of solid residue from COOL-process, *Chem. Ing. Tech.* 93 (11) (2021) 1833–1839.
- [66] M. Wang, Q. Tan, L. Liu, J. Li, A facile, environmentally friendly, and low-temperature approach for decomposition of polyvinylidene fluoride from the cathode electrode of spent lithium-ion batteries, *ACS Sustain. Chem. Eng.* 7 (15) (2019) 12799–12806.
- [67] B. Zheng, W. Zhou, H. Liu, S. Chen, P. Gao, Z. Wang, J. Liu, Surface chemistry induced robust SEI on graphite surface via soft carbon coating enables fast lithium storage, *Carbon* 218 (2024) 118729.
- [68] T. Otowa, R. Tanibata, M. Itoh, Production and adsorption characteristics of MAXSORB: high-surface-area active carbon, *Gas Sep. Purif.* 7 (4) (1993) 241–245.
- [69] F. Boi, C.Y. Lee, S. Wang, H. Wu, L. Li, L. Zhang, S. Grasso, Rhombohedral stacking-faults in exfoliated highly oriented pyrolytic graphite, *Carbon Trends* 15 (2024) 100345.
- [70] T. Cheng, S. Qi, Y. Jiang, L. Wang, Q. Zhu, J. Zhu, Z. He, Carbon structure regulation strategy for the electrode of vanadium redox flow battery, *Small* 20 (37) (2024) 2400496.
- [71] Y. Zhu, H. Liu, T. Wang, Y. Wang, H. Liu, Evolution of pore structures and fractal characteristics of coal-based activated carbon in steam activation based on nitrogen adsorption method, *Powder Technol.* 424 (2023) 118522.
- [72] Z. Tai, Q. Zhang, Y. Liu, H. Liu, S. Dou, Activated carbon from the graphite with increased rate capability for the potassium ion battery, *Carbon* 123 (2017) 54–61.
- [73] J. Serafin, B. Dziejarski, Ó.J. Fonseca-Bermúdez, L. Giraldo, R. Sierra-Ramírez, M. G. Bonillo, J.C. Moreno-Piraján, Bioorganic activated carbon from cashew nut shells for H₂ adsorption and H₂/CO₂, H₂/CH₄, CO₂/CH₄, H₂/CO₂/CH₄ selectivity in industrial applications, *Int. J. Hydrogen Energy* 86 (2024) 662–676.
- [74] J. Serafin, K. Kielbasa, B. Michalkiewicz, The new tailored nanoporous carbons from the common polypody (*Polypodium vulgare*): the role of textural properties for enhanced CO₂ adsorption, *Chem. Eng. J.* 429 (2022) 131751.
- [75] A.M. Haggag, A.A. Aboul-Enein, A.E. Awadallah, M.A. Azab, Novel concept for synthesizing carbon nano-onion, graphene layers, and graphene nano-ribbons from polypropylene waste over Fe₂O₃ nanoparticles, *Carbon Lett.* (2025) 1–13.
- [76] D.W. Boukhvalov, V.Y. Osipov, D. Murzalinov, A. Serikkanov, H. Bi, A comprehensive model of carbon nanodots with 0.21 nm lattice fringes patterns, *Carbon* 225 (2024) 119101.
- [77] D.W. Kim, H.S. Kil, J. Kim, I. Mochida, K. Nakabayashi, C.K. Rhee, S.H. Yoon, Highly graphitized carbon from non-graphitizable raw material and its formation mechanism based on domain theory, *Carbon* 121 (2017) 301–308.
- [78] V.R. Magri, C.S. de Matos, M.A. Rocha, C. Taviot-Gueho, V.R. Constantino, Pyrolysis of folic acid: Identification of gaseous/volatile products and structural evolution of N-doped graphitic carbon, *Thermochim. Acta* 739 (2024) 179813.
- [79] A. Marcilla, D. Berenguer, TGA/FTIR study of the decomposition of Heet tobacco in presence of zeolites and silicate compounds, *Mater. Sci. Eng. B* 295 (2023) 116593.
- [80] M. Feizbakhshan, Z. Hashisho, D. Crompton, J.E. Anderson, M. Nichols, Effect of activated carbon's pore size distribution on oxygen induced heel build-up, *J. Hazard. Mater.* 457 (2023) 126905.
- [81] I. Karnis, F. Krasanakis, L. Sygellou, A.N. Rissanou, K. Karatasos, K. Chrissopoulou, Varying the degree of oxidation of graphite: effect of oxidation time and oxidant mass, *PCBP* 26 (13) (2024) 10054–10068.
- [82] S. Gadipelli, Z.X. Guo, Graphene-based materials: synthesis and gas sorption, storage and separation, *Prog. Mater. Sci.* 69 (2015) 1–60.
- [83] D.J. Morgan. Comments on the XPS analysis of carbon materials. *C*, 7(3) 2021 51.
- [84] H. Arslanoğlu, Direct and facile synthesis of highly porous low cost carbon from potassium-rich wine stone and their application for high-performance removal, *J. Hazard. Mater.* 374 (2019) 238–247.
- [85] J. Wang, S. Kaskel, KOH activation of carbon-based materials for energy storage, *J. Mater. Chem.* 22 (45) (2012) 23710–23725.

- [86] M. Hu, Z. Ye, Q. Zhang, Q. Xue, Z. Li, J. Wang, Z. Pan, Towards understanding the chemical reactions between KOH and oxygen-containing groups during KOH-catalyzed pyrolysis of biomass, *Energy* 245 (2022) 123286.
- [87] R. Arunpandian, M. Kumar, P.Y. Yang, C.H. Chiang, J.H. Chang, Enhancing graphitization with desirable porosity for CO₂ adsorption through a one-step strategy and a novel stepwise pyrolysis method from Terminalia boivinii tul tree dead leaves, *Surf. Interfaces* 44 (2024) 103696.
- [88] S. Hu, S. Lin, D. Wen, Regulation of reactive oxygen species generation by graphitization and defect degree of Co-loaded carbon in peroxydisulfate activation, *Sep. Purif. Technol.* 354 (2025) 129195.